Process simulation-informed topology optimization for formwork-based concrete casting

Tong, Wei; Zhai, Xiaoya; Weng, Yiwei; Wu, Jun

DOI
10.1007/s00158-025-04084-x

Publication date
2025

Document Version
Final published version

Published in
Structural and Multidisciplinary Optimization

Citation (APA)
Tong, W., Zhai, X., Weng, Y., & Wu, J. (2025). Process simulation-informed topology optimization for formwork-based concrete casting. *Structural and Multidisciplinary Optimization*, *68*(8), Article 154. https://doi.org/10.1007/s00158-025-04084-x

Structural and Multidisciplinary Optimization (2025) 68:154
https://doi.org/10.1007/s00158-025-04084-x

RESEARCH PAPER

Process simulation-informed topology optimization for formwork-based concrete casting

Wei Tong[1] · **Xiaoya Zhai**[2] · **Yiwei Weng**[1] · **Jun Wu**[3]

Received: 24 March 2025 / Revised: 2 June 2025 / Accepted: 3 July 2025

Abstract

Concrete casting, a cornerstone of construction, relies on formwork to shape structures and has been used to create topology-optimized lightweight designs. The interplay between cast structures and formwork necessitates balancing casting constraints, particularly filling efficiency in topological channels, to avoid defects that compromise performance. However, filling efficiency is often empirically addressed, limiting optimization potential. Traditional methods require extensive post-processing to improve filling efficiency, increasing costs and design time. This work introduces a process simulation-informed reverse topology optimization framework, integrating casting constraints into the design process. The framework combines topology optimization, Discrete Element Method (DEM) simulation, and filling ratio identification. Its effectiveness is demonstrated through 2D numerical examples, experimental validation, and a preliminary 3D extension. Results show that the optimized structures improve filling efficiency and allow customizable casting positions. This approach offers a novel strategy for formwork optimization, enhancing efficiency and reducing costs in the building industry.

Keywords Formwork · Topology optimization · Manufacturing constraints · DEM · Casting design

1 Introduction

Concrete casting has been widely used in construction to fabricate complex building structures. Formwork is essential in the casting process to achieve the desired geometries. Formwork refers to the temporary or permanent molds or structures that shape and support concrete or similar materials. It helps create the structures using precast or cast-in-place methods. As sustainable low-carbon buildings advance, lightweight cast structures with minimal material and maximum stiffness have attracted significant attention in the building industry (Aghaei-Meibodi et al. 2017; Gaganelis and Mark 2019; Jipa et al. 2016; Søndergaard et al. 2018). The formwork for lightweight structures typically incorporates intricate flow pathways. Due to the inherent variability in material compositions and properties, complex formwork frequently leads to regions where the cast fails to achieve proper self-compaction, resulting in voids or inadequate density in localized areas (Mechtcherine et al. 2014). The complexity of the formwork makes it challenging to resolve this issue using conventional engineering methods, such as vibration compaction. Therefore, a novel approach is needed to integrate casting constraints into structural design, enabling the structural formwork to achieve self-compacting casting.

Topology optimization is a promising approach to achieving optimal lightweight structures. This computational method allows for the precise distribution of material within a given design space to meet specific performance criteria, such as stiffness and strength, while minimizing material use (Sigmund and Maute 2013). In civil and building engineering, some building examples include the Qatar National Convention Centre in Doha (Isozaki 2011), the Shanghai Himalayas Center in China (Isozaki 2010), “Xiong'an Wings” in China (under construction) (Li et al. 2023), etc. Furthermore, designers can create various functional structures by applying different topology optimization methods

Responsible editor: Makoto Ohsaki

✉ Yiwei Weng
yiwei.weng@polyu.edu.hk

[1] Department of Building and Real Estate, The Hong Kong Polytechnic University, Hong Kong 999077, China

[2] School of Mathematical Sciences, University of Science and Technology of China, Hefei, Anhui 230026, China

[3] Department of Sustainable Design Engineering, Delft University of Technology, Delft 2628 CE, The Netherlands

(Stoiber and Kromoser 2021) and construction techniques, such as prestressed topological concrete structures (Ooms et al. 2022), cable-supported topological structures (Li et al. 2024), etc. Topology optimization provides designers with the freedom to create aesthetically pleasing and functional forms.

There are two primary technologies for producing topology-optimized concrete structures: 3D concrete printing (3DCP) and formwork casting. 3DCP is a technique that builds objects by successively depositing concrete material layer by layer (Zhuang et al. 2024a). Due to the intrinsic characteristics of the manufacturing process, complex optimized structures often need to be printed and assembled in batches to avoid print failures (Vantyghem et al. 2020). Furthermore, the inter-layer bonding tends to weaken due to cold-joint effects (Ma et al. 2019). In contrast, formwork casting, as a traditional method, offers superior strength and consistency. The flexibility and stability of formwork casting make it the preferred method for producing topology-optimized structures, especially in designs requiring large overhangs or high performance (Jipa et al. 2016, 2019).

Although formwork casting is widely favored, it still has some limitations. In the building industry, casting materials exhibit different compositions and flowability (Jiao et al. 2017; Revilla-Cuesta et al. 2023). In particular, concrete materials with high yield stress or the inclusion of coarse aggregates exhibit reduced flowability, which results in inadequate filling during the casting process (Roussel 2007). The limited fluidity impairs the ability to flow smoothly into all voids and cavities, potentially causing incomplete or uneven distribution. Moreover, this distribution is related to the location of the casting, as shown in Fig. 1. As the complexity of formwork increases, the improper filling issue becomes even more critical. Therefore, addressing the filling challenges of complex formwork is extremely important for promoting application of topology-optimized structures in the building industry.

Regarding the filling issue, there is relevant research in materials science. Firstly, enhancing the flowability of the casting material is a potential solution for improving filling efficiency. However, high-flow materials are more expensive than traditional ones (Gaimster and Dixon 2003), and study shows that they still fail to effectively fill complex voids due to the presence of aggregates (Zhang et al. 2020). Secondly, numerical methods can be used to predict material filling behavior, among which the Discrete Element Method (DEM) is a feasible approach to simulating the flow of particle materials (Mechtcherine et al. 2014). Zhang et al. (2020) analyzed the filling capacity of self-compacting concrete (SCC) with DEM. Yan et al. (2022) and Li et al. (2021) simulated the flowability of fresh concrete using Hertz–Mindlin with the Johnson–Kendall–Roberts (JKR) model. However, this method is limited to forward prediction of formwork-filling behavior before casting and does not support automatic reverse adjustment of the formwork geometry.

In topology optimization, incorporating design constraints into computational design has become a significant and increasingly active area of research. Stress constraints based on concrete yield criteria are incorporated into topology optimization (Bogomolny and Amir 2012; Jewett and Carstensen 2019; Luo et al. 2012). Amir and Sigmund (2013) developed a reinforcement layout optimization method for concrete structures with a continuum damage model. Subsequently, Smarslik et al. (2019) proposed a topology optimization method that biases concrete designs toward tension or compression, extending to truss and truss-continuum optimization. The optimization of concrete structures described above can be categorized into mechanics-based constraints and performance-driven optimization; however, they neglect the limitations of practical manufacturing. Manufacturing-driven topology optimization has also been investigated in recent years. The length scale constraints have been extensively investigated to address size requirements across various manufacturing conditions (Fernández et al. 2020; Guest 2009; Zhou et al. 2015). Langelaar (2016; 2017) incorporated the constraints of additive manufacturing into topology optimization. Wu et al. (2017a, b) introduced local volume constraints to

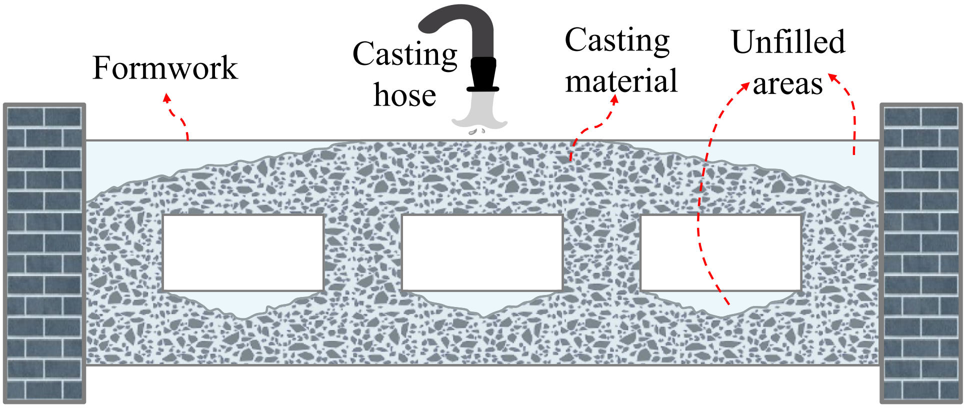

Fig. 1 Illustration of improper filling of formwork with casting

generate porous structures. Wang et al. (2020b) considered the manufacturing sequence constraint to optimize the structural layout. Additionally, casting constraints have also been considered in topology optimization to eliminate undercuts and internal cavities, facilitating demolding after hardening (Li et al. 2018; Wang et al. 2020a; Wang et al. 2023; Xia et al. 2011). However, unlike existing casting constraints, this work primarily focuses on the constraint of casting filling efficiency in the manufacturing process.

Incorporating the geometric characteristics of the casting process into computational design is a potential strategy for optimizing the effectiveness of material filling. This work aims to develop a novel automated optimization framework to address the casting issue in topology-optimized formwork. The whole framework consists of three main components: (i) a DEM particle filling simulation module developed upon an existing framework, (ii) a topology optimization module with casting geometry constraints, and (iii) a filling rate identification module based on image processing techniques. The proposed framework optimizes the filling rate and structural compliance by iteratively adjusting geometrically constrained characteristics through a continuous topology optimization strategy. It enhances structural manufacturability and integrity while maximizing stiffness, reducing the risks associated with improper filling.

The remainder of this article is organized as follows: Sect. 2 introduces the computational method of the proposed optimization framework. The numerical tests and discussion are provided in Sect. 3. An experimental test is presented in Sect. 4. Section 5 demonstrates a preliminary attempt to extend the framework from 2D to 3D. Finally, a conclusion is provided in Sect. 6.

2 Computational method

2.1 Geometric characteristics for casting

According to research (Banfill 2011; Felekoğlu et al. 2007; Hu and Wang 2011) on fresh concrete materials, flowability is influenced by several factors, including the water-cement ratio, admixtures, aggregate size and grading, etc. However, existing research on concrete casting into complex formwork has not been extensively studied.

Based on engineering experience and flow tests, two notable geometric characteristics of concrete flow can be summarized. First, the L-box test indicates that concrete materials tend to form an inclined unfilled region during flow (Hosseinpoor et al. 2017; Nguyen et al. 2006; Onyelowe et al. 2022; Shan et al. 2015), which can be simplified as an angle of repose θ as shown in Fig. 2a. Secondly, when aggregates flow through a narrower space, they are more likely to experience flow obstruction due to wall friction or particle clogging, as illustrated in Fig. 2b. This phenomenon is a primary cause of pipeline blockage during concrete pumping (Secrieru et al. 2020) and extrusion (El Cheikh et al. 2017).

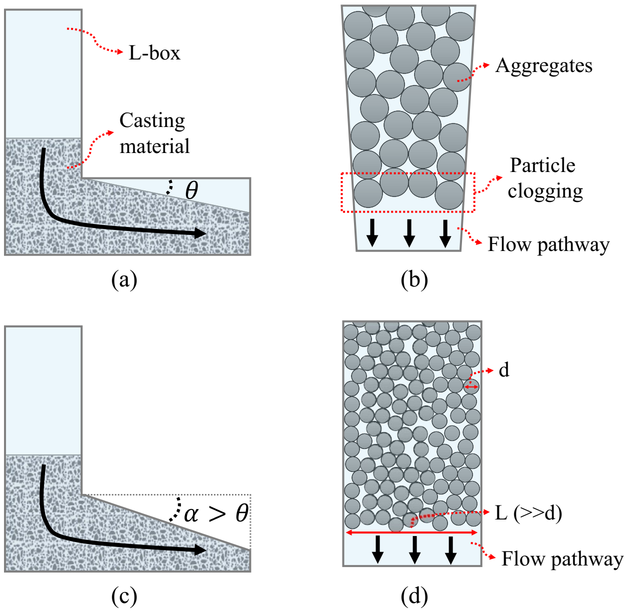

Fig. 2 **a** Simplified concrete profile in L-box; **b** Illustration of particle clogging in flow pathway; **c** and **d** Proposed geometry designs for proper casting

In summary, incorporating a sloped design in the horizontal channels (Fig. 2c) and ensuring the flow path width is significantly greater than the particle diameter (Fig. 2d) can effectively facilitate the casting process.

2.2 Topology optimization formulation

This section aims to introduce the geometric constraints summarized in Sect. 2.1 into the topology optimization process, ensuring that the final optimized structures possess the desired geometric characteristics for casting. The method presented in this section is for the optimization of 2D structures; however, its extension to 3D is straightforward and is briefly illustrated in Sect. 5.

2.2.1 Casting filter formulation

In the casting process, the casting position would influence the flow dynamics of the material, leading to variations in the angle of repose (θ). As shown in Fig. 3, to facilitate the integration of angle θ into topology optimization, the design domain is discretized into uniform rectangular finite elements with dimensions $l_x \times l_y$. The angle θ can be mathematically represented in terms of the element dimension:

Fig. 3 A simplified illustration of θ with casting opening (left) and finite element representation (right)

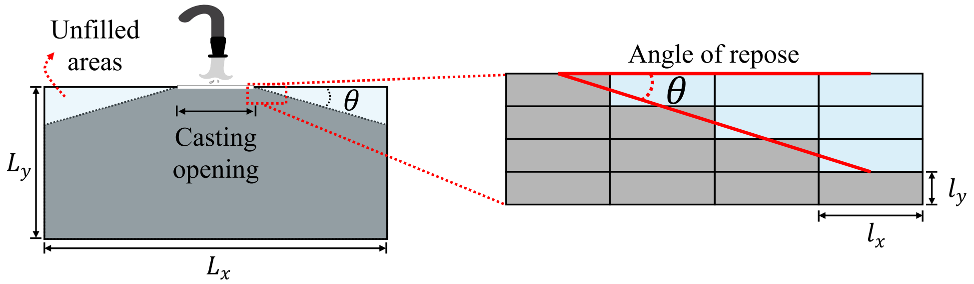

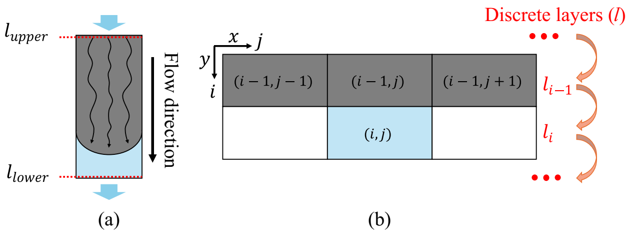

(a) (b)

Fig. 4 **a** Material migration process versus time; **b** Illustration of process-dependent material migration process in finite element mesh

$$\theta = \arctan\left(l_y/l_x\right) \tag{1}$$

The value of θ is adjusted by altering the finite element's aspect ratio (l_y/l_x). In this work, l_x is assigned as a constant value for each example, while variations in l_y are used to achieve changes in θ. Therefore, the entire design domain is discretized into $n_x \times n_y$ rectangular elements along the xy-coordinate axes.

$$n_x = \lfloor L_x/l_x \rfloor; n_y = \lfloor L_y/l_y \rfloor \tag{2}$$

where L_x and L_y are the total length and height of the design domain, and the "$\lfloor \ \rfloor$" represents the floor function (i.e., rounding a number down to the nearest integer).

During the casting process, the material enters the formwork through an opening and progressively flows downward under gravity. As demonstrated in Fig. 4a, the material preferentially flows through the upper layer (l_{upper}) before reaching the lower layer (l_{lower}). In other words, if no material passes within the upper neighboring threshold of a region, then its lower region cannot be filled. It demonstrated the process-dependent and hierarchical nature of the material flow process, where each region's filling relies on the proper migration of material in the area above it.

As mentioned earlier, the flow region is discretized using regular meshes, as depicted in Fig. 4b. Such a regular element facilitates the straightforward implementation of the filtering strategy. The density of each element is represented as a continuous variable within the range of [0,1]. Here, $\rho_{c(i,j)}$ denotes the actual cast density, where the footnotes i and j represent the element's position in the y and x directions, respectively. A dependency rule can describe the flow behavior within a finite element mesh, wherein the filling feasibility of a lower blue element (i,j) is governed by the maximum density of its three adjacent upper elements, which is:

$$\begin{aligned} &\rho_{c(i,j)} \leq \max\left(\rho_{c(i-1,j-1)}, \rho_{c(i-1,j)}, \rho_{c(i-1,j+1)}\right); \\ &i \in \{1,2,\ldots,n_y\}, j \in \{1,2,\ldots,n_x\} \end{aligned} \tag{3}$$

The structural optimization presented in this work is conducted under the assumption of regular discretization. Therefore, it may be less effective in accurately representing complex curved geometric boundaries. Although this limitation is acknowledged in topology optimization, the regular voxel grid facilitates the mathematical definition and implementation of the proposed filtering strategy.

Each element is initially assigned a density variable in topology optimization, defined as the blueprint density $\rho_{(i,j)}$. The blueprint density $\rho_{(i,j)}$ may violate the condition in Eq. (3), thus a method is required to process $\rho_{(i,j)}$ to satisfy the constraint. Here, a "casting filter" is proposed, and Fig. 5 illustrates the computation procedure of the filtering method. For element (i,j), the actual cast density $\rho_{c(i,j)}$ can be formulated in terms of the blueprint density $\rho_{(i,j)}$ and the castable density $\rho_{b(i,j)}$. The castable density $\rho_{b(i,j)}$ is defined as the maximum value that satisfies the inequality condition described in Eq. (3). Mathematically, the casting filter is expressed as:

$$\rho_{c(i,j)} = \min\left(\rho_{(i,j)}, \rho_{b(i,j)}\right) \tag{4}$$

$$\rho_{b(i,j)} = \max\left(\rho_{c(i-1,j-1)}, \rho_{c(i-1,j)}, \rho_{c(i-1,j+1)}\right) \tag{5}$$

A differentiable Boltzmann operator (Asadi and Littman 2017) is employed to get a smooth approximation of maximum and minimum functions:

$$\min : \rho_{c(i,j)} \approx \frac{\sum\limits_{x \in \{\rho,\rho_b\}} x \exp\left(\alpha_{\min} x\right)}{\sum\limits_{x \in \{\rho,\rho_b\}} \exp\left(\alpha_{\min} x\right)} \tag{6}$$

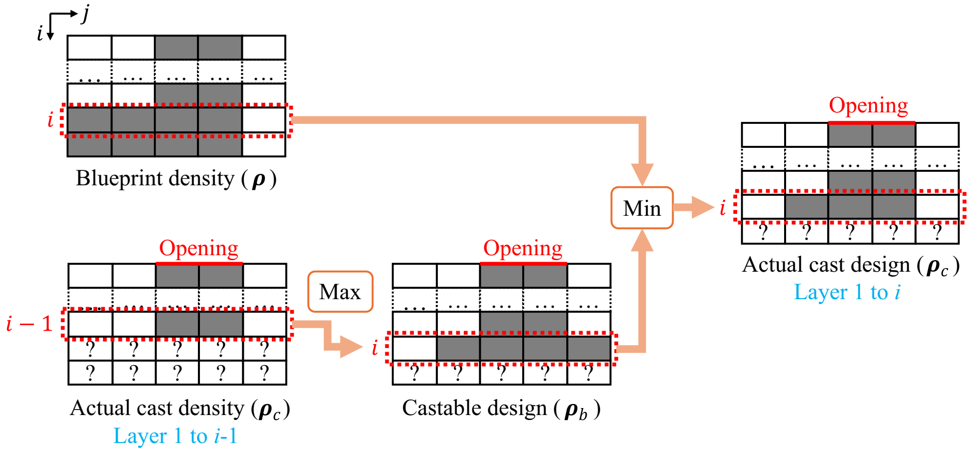

Fig. 5 Graphical explanation of casting filter

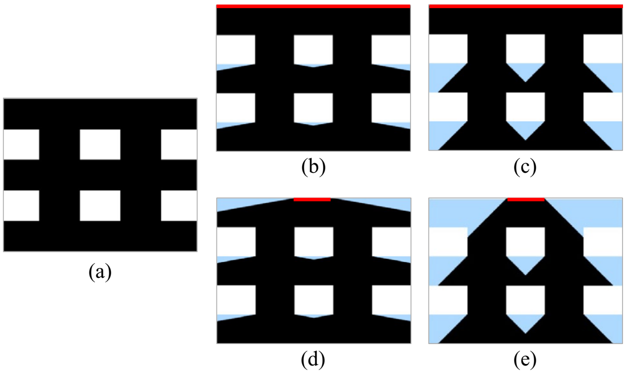

Fig. 6 Effectiveness tests of the casting filter with different opening configurations; the opening locations are highlighted in red. **a** Original density pattern; **b** and **d** Filtered density with $\theta = 10°$; **c** and **e** Filtered density with $\theta = 45°$

$$\max\ :\ \rho_{b(i,j)} \approx \frac{\sum_{x\in\boldsymbol{\rho}_c} x\exp\left(\alpha_{\max}x\right)}{\sum_{x\in\boldsymbol{\rho}_c} \exp\left(\alpha_{\max}x\right)} \tag{7}$$

where $\alpha_{\min}$ and $\alpha_{\max}$ are tuning parameters governing the balance between smoothness and accuracy. As $\alpha_{\min}$ approaches $-\infty$ and $\alpha_{\max}$ approaches $+\infty$, ρ_c and ρ_b converge to the minimum and maximum value, respectively. However, a much greater absolute value would increase the nonlinearity and lead to instability. In this paper, the following values are used:

$$\alpha_{\min} = -25; \alpha_{\max} = 25 \tag{8}$$

The proposed casting filter's effectiveness has been tested before topology optimization. Figure 6 depicts the density field after employing the proposed casting filter for different opening locations and angles of repose θ. It demonstrated that the regions identified as difficult to fill are suppressed, shown in blue.

2.2.2 Stiffness matrix with angle of repose (θ) control

Classical 2D topology optimization algorithms usually use square elements as fundamental elements, which does not allow for adaptive angle control. As expressed in Eq. (1), the angle of repose θ will be controlled by changing the element aspect ratio. In finite element analysis (FEA), the change in the shape of an element will lead to a change in the element stiffness matrix ($\mathbf{k}_0$), which can be determined as:

$$\mathbf{k}_0 = \int_{\Omega} \mathbf{B}^{\top}\mathbf{D}\mathbf{B}\,d\Omega \tag{9}$$

where $\mathbf{B}$ is the strain–displacement matrix, $\mathbf{D}$ is the elasticity matrix, and Ω is the integration region of the element. Detailed information can be found in FEA textbooks (Bhavikatti 2005; Szabó and Babuška 2021), and the expressions of $\mathbf{B}$ and $\mathbf{D}$ are presented simply in Appendix A.

2.2.3 Four-field scheme

An optimization flowchart is provided in the orange block of Fig. 7. The first field $\mathbf{x}$ represents the design density variables of topology optimization. A smoothing filter is introduced to eliminate checkerboard patterns and guarantee well-posed and mesh-independent solutions (Andreassen et al. 2011; Sigmund 2007). The smoothing density field $\mathbf{x}_s$ is explicitly defined as:

$$\mathbf{x}_s = \mathbf{H}_s\mathbf{x} \tag{10}$$

where $\mathbf{H}_s$ is the weighted convolution matrix for the adaptive rectangular mesh, the entry in the u-th row and v-th column of $\mathbf{H}_s$ matrix is determined as:

$$\left(\mathbf{H}_s\right)_{u,v} = \frac{H_{uv}}{\sum_{v'\in N_u} H_{uv'}} \tag{11}$$

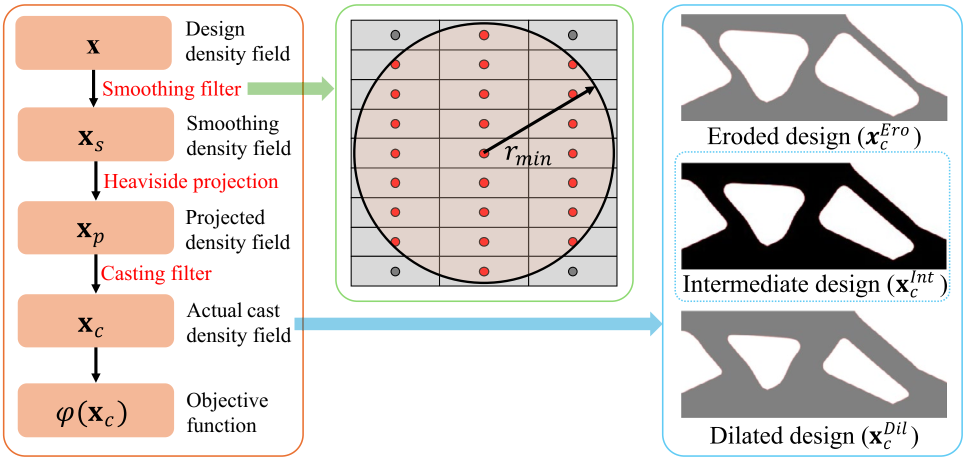

Fig. 7 Illustration of four-field scheme (left), smoothing filter for rectangular mesh (middle), and the final three designs by employing the robust formulation (right)

$$H_{uv} = \max(0, r_{\min} - \Delta(u, v)) \tag{12}$$

where N_u is the set of elements v within a circle where its centroid-to-centroid distance to element u is less than the radius $r_{\min}$ (i.e., $\Delta(u,v) < r_{\min}$), as shown in the green block in Fig. 7. In the optimization process, the filter radius $r_{\min}$ remains constant when the mesh size changes to ensure consistent filtering.

A threshold projection is applied to drive the smoothed density field $\mathbf{x}_s$ toward a binary solution {0,1}, thereby reducing intermediate density regions (Sigmund 2007). The projected density field $\mathbf{x}_p$ is obtained by using the differentiable Heaviside function:

$$\mathbf{x}_p = \frac{\tanh(\beta\eta) + \tanh\left[\beta\left(\mathbf{x}_s - \eta\right)\right]}{\tanh(\beta\eta) + \tanh\left[\beta(1 - \eta)\right]} \tag{13}$$

where η and β are the threshold and sharpness control parameters. As β tends to $+\infty$, $\mathbf{x}_p$ tends to the binomial distribution.

Finally, the casting filter proposed in Sect. 2.2.1 is applied to perform filtering operations on the projected density field $\mathbf{x}_p$ to obtain the actual cast density field $\mathbf{x}_c$. Therefore, a four-evolutionary density process is created: $\mathbf{x} \rightarrow \mathbf{x}_s \rightarrow \mathbf{x}_p \rightarrow \mathbf{x}_c$. The optimization function φ is defined in terms of the final field $\mathbf{x}_c$.

2.2.4 Optimization problem with robust formulation

As mentioned in Sect. 2.1, apart from the angle of repose θ, another geometric factor is the size of the channel. Narrow channels would obstruct flow and increase the complexity of formwork manufacturing. To prevent this, a robust formulation (Sigmund 2009; Wang et al. 2011) is adapted to reduce the generation of small length scale components. The robust formulation is based on the eroded, intermediate, and dilated designs. The optimization focuses on the worst-performing structure of the objective function in each iteration.

The compliance minimization problem is considered in this paper, which is defined as follows:

$$\begin{aligned} \min_{\mathbf{x}} &: \max\left(C\left(\mathbf{x}_c^{Ero}(\mathbf{x})\right), C\left(\mathbf{x}_c^{Int}(\mathbf{x})\right), C\left(\mathbf{x}_c^{Dil}(\mathbf{x})\right)\right) \\ \text{S.t.} &: V\left(\mathbf{x}_c^{Int}\right) \le fV_0 \\ & \mathbf{K}(\mathbf{x}_c^{Ero})\mathbf{U}^{Ero} = \mathbf{F} \\ & \mathbf{K}(\mathbf{x}_c^{Int})\mathbf{U}^{Int} = \mathbf{F} \\ & \mathbf{K}(\mathbf{x}_c^{Dil})\mathbf{U}^{Dil} = \mathbf{F} \\ & \mathbf{0} \le \mathbf{x} \le \mathbf{1} \end{aligned} \tag{14}$$

where the superscripts *Ero*, *Int*, and *Dil* represent erosion, intermediate, and dilation, respectively. C is the compliance ($C = \mathbf{F}^{\mathbf{T}}\mathbf{U}$), $\mathbf{F}$ and $\mathbf{U}$ are the global node force vector and displacement vector, $V(\mathbf{x}_c)$ and V_0 denote the total material volume and design domain volume, and f is the user-defined volume fraction of the design domain. $\mathbf{K}$ is the global stiffness matrix assembled from all the element stiffness matrices $\mathbf{k}_{(i,j)}$. The element stiffness matrix $\mathbf{k}_{(i,j)}$ is computed as:

$$\mathbf{k}_{(i,j)} = E_{(i,j)}\mathbf{k}_0(v) \tag{15}$$

where $\mathbf{k}_0$ is the element stiffness matrix in terms of unit Young's modulus and Poisson's ratio v, $E_{(i,j)}$ is Young's modulus of element (i,j) interpolated by the solid (E_0) and void ($E_{\min}$) stiffness. For the (i,j)-th element in the actual cast density field $x_{c(i,j)}$, $E_{(i,j)}$ is expressed as:

$$E_{(i,j)} = E_{\min} + \left(x_{c(i,j)}\right)^P \left(E_0 - E_{\min}\right); \left(x_{c(i,j)} \in \mathbf{x}_c\right) \tag{16}$$

where P is a penalization factor; a constant value of $P = 3$ is employed, as it can yield favorable outcomes and align effectively with the stiffness properties of multiphase materials (Bendsoe and Sigmund 2003).

For a robust formulation, three finite element problems are required to solve. The eroded ($\mathbf{x}_c^{Ero}$), intermediate

($\mathbf{x}_c^{Int}$), and dilated ($\mathbf{x}_c^{Dil}$) designs are obtained by utilizing Heaviside projection in Eq. (13) with thresholds of 1-η, 0.5, and η ($0 \leq \eta \leq 0.5$). The blue block in Fig. 7 shows the three results of the robust design of a beam. Unlike the work of Wang et al. (2011), this study applies the robust formulation to the actual cast density ($\mathbf{x}_c$) rather than the projected density ($\mathbf{x}_p$). It should be emphasized that the casting filter does not preserve the length scale, and therefore, it cannot strictly guarantee the minimum length scale for the intermediate design $\mathbf{x}_c^{Int}$. However, this approach allows for the elimination of small length scale components prior to performing the casting filter, resulting in a reasonable and lower-complexity final structure. Furthermore, the volume constraint is imposed on the intermediate design density ($\mathbf{x}_c^{Int}$), corresponding to the structure to be manufactured.

The sensitivities of the objective and constraint functions are required for gradient-based optimization. The gradient information is elaborated on in Appendix B. The method of moving asymptotes (MMA) solver (Svanberg 1987) is used to update the design density $\mathbf{x}$ based on sensitivities.

2.3 Discrete element method (DEM)

This section presents the methodologies of a simplified DEM model for particle flow simulations, intending to perform a preliminary evaluation of the topology-optimized structures. The particle contact constitutive model is custom-developed and built upon the MatDEM framework (Liu et al. 2021). The particle filling results obtained from the DEM simulations can be used as indicators for updating the geometric constraint parameters in topology optimization.

2.3.1 Particle Kinematics

The particle translation is determined by Newton's Second Law of Motion, which is given by:

$$F_\kappa = m_\kappa \left(\ddot{s}_\kappa - g_\kappa \right) \tag{17}$$

where F_κ is the (non-gravitational) resultant force on particle κ, m_κ is the particle's mass, $\ddot{s}_\kappa$ is the translational acceleration, and g_κ is the gravitational acceleration. The translational acceleration at time t can be expressed in terms of the particle's velocity ($\dot{s}_\kappa$) by the central finite difference method:

$$\ddot{s}_\kappa^t = \left(\dot{s}_\kappa^{t+\Delta t/2} - \dot{s}_\kappa^{t-\Delta t/2} \right) / \Delta t \tag{18}$$

Based on Eq. (17)&(18), the particle's velocity can be determined. Then, the displacement (s_κ) at time $t + \Delta t$ is updated as follows:

$$s_\kappa^{t+\Delta t} = s_\kappa^t + \dot{s}_\kappa^{t+\Delta t/2} \Delta t \tag{19}$$

2.3.2 Hertz–Mindlin with Johnson-Kendall-Roberts (JKR) model

The casting materials are typically cohesive wet materials. Therefore, the Hertz–Mindlin with JKR model is adopted to capture the effects of Van der Waals forces within the contact zone and model adhesive systems. As shown in Fig. 8, this contact constitutive model includes normal force (F_N), tangential force (F_T), normal damping force (F_{ND}), tangential damping force (F_{TD}), and friction force (F_μ).

The normal force is based on the JKR theory (Johnson et al. 1971). It depends on the normal overlap δ_n and the interaction parameter, which is given by:

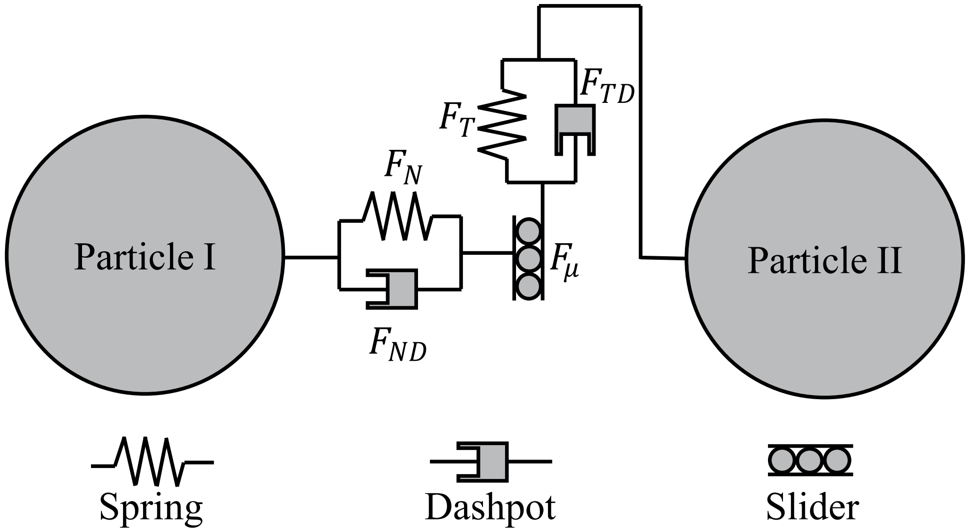

Fig. 8 Schematic diagram of Hertz–Mindlin with JKR model

$$F_N = -4\sqrt{\pi\gamma E^*}a^{3/2} + \frac{4E^*}{3R^*}a^3 \tag{20}$$

where γ is the surface energy, a is the contact patch radius, E^* and R^* are the equivalent Young's modulus and equivalent radius, respectively. For particles I and II with Young's modulus E_{I}, E_{II}, Poisson's ratios v_{I}, v_{II}, and radius R_{I}, R_{II}, the equivalent Young's modulus and equivalent radius are defined as follows:

$$\frac{1}{E^*} = \frac{(1 - v_{\mathrm{I}}^2)}{E_{\mathrm{I}}} + \frac{(1 - v_{\mathrm{II}}^2)}{E_{\mathrm{II}}} \tag{21}$$

$$\frac{1}{R^*} = \frac{1}{R_{\mathrm{I}}} + \frac{1}{R_{\mathrm{II}}} \tag{22}$$

The contact patch radius (a) that is related to normal overlap δ_N, which is expressed implicitly as:

$$\delta_N = \frac{a^2}{R^*} - \sqrt{\frac{4\pi\gamma a}{E^*}} \tag{23}$$

since solving the Eq. (23) for contact patch radius is not trivial, an approximate explicit expression is employed in this work (Chen et al. 2023), which is provided in Appendix C.

The tangential force is based on the work of Mindlin and Deresiewicz (1953), which depends on the tangential overlap (δ_T) and the tangential stiffness (S_T) between particles. It gives:

$$F_T = -S_T\delta_T \tag{24}$$

where

$$S_T = 8G^*a \tag{25}$$

G^* is the equivalent shear modulus. For particles I and II with shear modulus G_{I} and G_{II}, G^* is computed as:

$$\frac{1}{G^*} = \frac{2 - v_{\mathrm{I}}}{G_{\mathrm{I}}} + \frac{2 - v_{\mathrm{II}}}{G_{\mathrm{II}}} \tag{26}$$

where G_{I} and G_{II} are determined by using the well-known relation between the elastic constants, $G_{\mathrm{I}} = E_{\mathrm{I}}/2(1 + v_{\mathrm{I}})$ and $G_{\mathrm{II}} = E_{\mathrm{II}}/2(1 + v_{\mathrm{II}})$.

The tangential force is constrained by Coulomb friction (Cundall and Strack 1979), while the friction force is defined as:

$$F_\mu = \mu \cdot F_N \tag{27}$$

where μ is the friction coefficient. When $F_T \le \mu \cdot F_N$, the static friction force equals the applied tangential force, and the surfaces do not move relative to each other. When $F_T > \mu \cdot F_N$, the friction force reaches its maximum static value and then transitions to a constant kinetic friction force $\mu \cdot F_N$ once sliding begins.

The normal damping force and tangential damping force are defined as (Coetzee 2020):

$$F_{ND} = -2\xi_N\sqrt{S_N m^*}\dot{s}_{N(rel)} \tag{28}$$

$$F_{TD} = -2\xi_T\sqrt{S_T m^*}\dot{s}_{T(rel)} \tag{29}$$

where m^* is the equivalent mass, $\dot{s}_{N(rel)}$ and $\dot{s}_{T(rel)}$ are normal and tangential components of the relative velocity, S_N is the normal stiffness, ξ_N and ξ_T are normal and shear critical damping coefficients. Small damping coefficients are suggested for the dynamic simulation of casting (Liu 2019), and values of 0.01% are employed in this study. m^* and S_N are defined as follows:

$$\frac{1}{m^*} = \frac{1}{m_{\mathrm{I}}} + \frac{1}{m_{\mathrm{II}}} \tag{30}$$

$$S_N = 2E^*a \tag{31}$$

where m_{I} and m_{II} are the masses of the two contacting particles.

2.4 DEM simulation

2.4.1 Optimized geometry processing

In DEM simulation, smooth boundaries are more favorable for particle flow. However, due to the use of a density-based topology optimization method with rectangular elements, the resulting structures exhibit both grayscale values and jagged boundaries (Fig. 9b). To address this issue, a post-processing method is applied to extract smooth and well-defined boundaries of the actual cast density field ($\mathbf{x}_c$). For 2D boundary extraction, the built-in MATLAB function "contourf" is employed to generate contour lines at a specified density threshold value (0.5 in this work). This effectively delineates the interface between solid and void regions.

Figure 9a clearly illustrates an example of the boundary before and after post-processing. The red boundaries in Fig. 9c represent the post-processed contours of the topology-optimized structure, which are subsequently used to define the interface between the castable region and the formwork in the DEM simulations.

2.4.2 Casting opening configuration

The transition from the topology-optimized structure to the DEM casting simulation is straightforward. As shown in Fig. 10a, after the post-processing described in

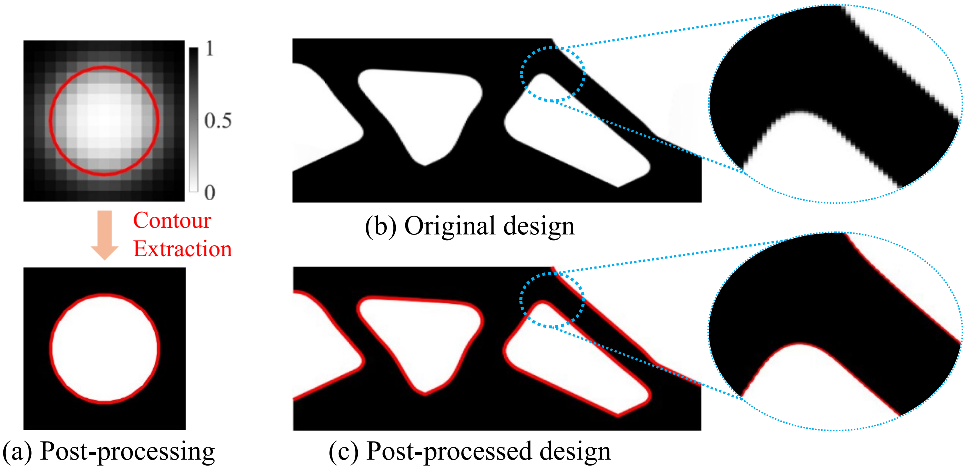

(a) Post-processing (b) Original design (c) Post-processed design

Fig. 9 Boundary post-processing of topology-optimized structure

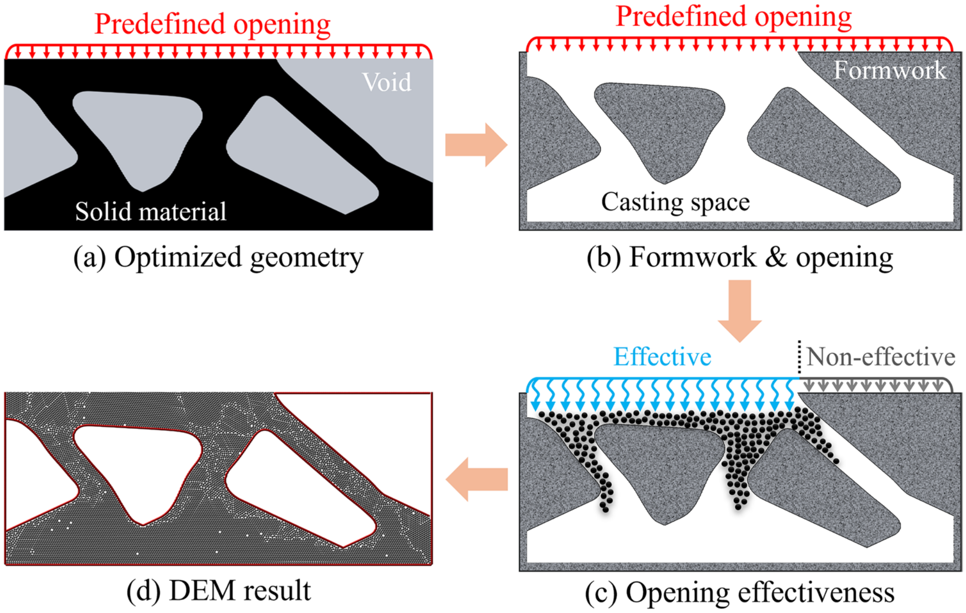

(a) Optimized geometry (b) Formwork & opening (c) Opening effectiveness (d) DEM result

Fig. 10 Illustration of casting opening configuration in DEM

Sect. 2.4.1, the optimized solid and void domains can be obtained under the predefined boundary conditions. The casting formwork is treated as the complementary structure of the optimized design; that is, the solid and void domains are inverted relative to Fig. 10a, as illustrated in Fig. 10b.

It should be noted that the predefined opening represents the maximum admissible inlet for particle injection. However, due to the material redistribution during topology optimization, some parts of the predefined opening may become blocked. As shown in Fig. 10c, although the particle opening was predefined along the entire upper boundary, only the left portion remains effective in the DEM simulation (indicated by blue arrows). The right portion is considered non-effective (indicated by gray arrows), through which particles are not allowed to enter the formwork. Figure 10d shows the final particle filling result from the DEM simulation.

2.5 Filling ratio identification

The purpose of determining the particle fill ratio in a formwork during DEM simulations is to evaluate how effectively the particles occupy the available space within the formwork, which can be used to guide topology optimization.

In DEM simulation, small gaps inevitably arise due to the packing of particles. Additionally, both dense and loose packing configurations can occur between particles, as shown in Fig. 11a. Here, it is defined that as long as the particles do not form large voids, the space is considered fully filled. A morphological opening operation is applied to analyze the DEM simulation results, where minor interparticle voids are neglected, and only larger voids, which may significantly affect material flow and compaction, are preserved for further evaluation. Figure 11b demonstrates a processed result: the black area (A_{black}) is identified as the

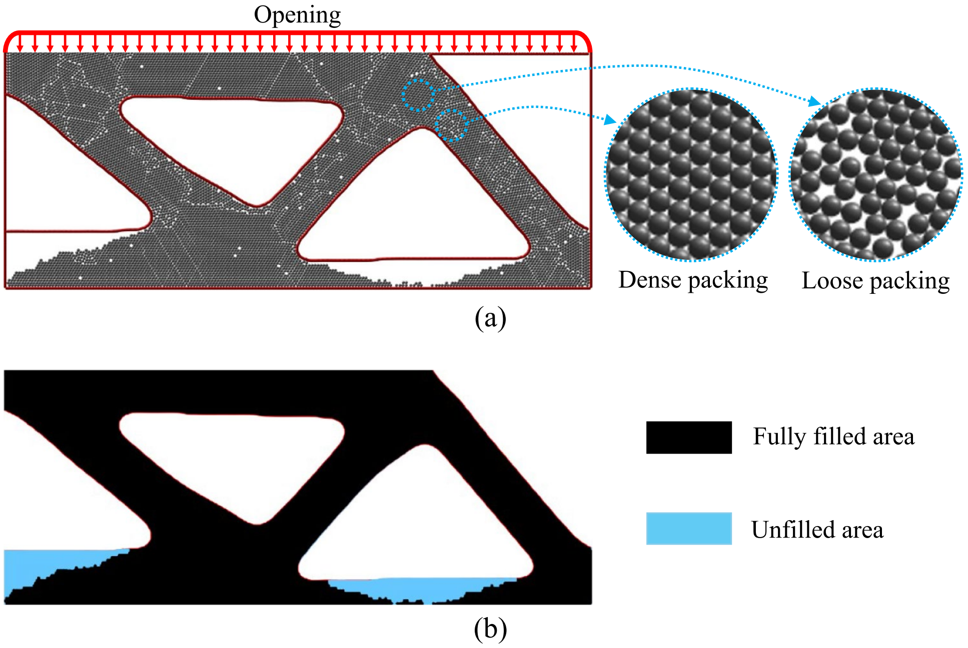

(a)

(b)

Fig. 11 **a** DEM simulation result for topology-optimized MBB beam; **b** Filling area identification using image processing with morphological opening operation

fully filled area, while the blue area (A_{blue}) is the unfilled area. The filling ratio (FR) is defined as:

$$FR = \frac{A_{black}}{A_{total}} \times 100\% \tag{32}$$

where A_{total} is the total area of the formwork, $A_{total} = A_{black} + A_{blue}$.

2.6 Numerical implementation

Figure 12 illustrates the proposed process simulation-informed topology optimization framework. The entire process is implemented in MATLAB R2024a to enable automated iterations. The algorithm of the proposed method is the following:

(1) Define the optimization problem and parameters. Note that the value of the filtering radius $r_{\min}$ (Eq. (12)) should not be small to avoid the generation of the small length scale components.
(2) Start topology optimization using the conventional method (i.e., without casting filter).
(3) Perform DEM simulations to determine the fill ratio of the structure obtained by the conventional method.
(4) Determine whether the fill ratio meets the desired criteria.
(5) If the topology obtained by the conventional method fails to achieve the desired filling criteria, the proposed method is employed.
(6) Start topology optimization using the four-field scheme with the rectangular mesh.
(7) Perform DEM simulations and filling ratio analysis.
(8) If the desired filling criteria are met, stop. Otherwise, remesh (i.e., increase mesh θ) and iterate from step 6.

The entire optimization framework consists of three main modules: the topology optimization module, the DEM simulation module, and the filling ratio analysis module. There are two types of variables involved in the optimization: the design density variables $\mathbf{x}$ and the angle θ. It is important to note that sensitivity analysis is performed only with respect to $\mathbf{x}$ within the topology optimization module. The angle θ is a predefined input to the topology optimization module. Therefore, the sensitivity analysis does not include derivatives of θ.

In this work, the parameter θ is updated heuristically based on the results of the DEM simulation. A continuation strategy is adopted, and the topology optimization is initiated with a mesh and an initial θ of 15°. If the convergence criteria are not met, θ is incrementally increased by $\Delta = +5^\circ$ at the next iteration until convergence is achieved.

This heuristic approach is based on an engineering intuition: a larger channel inclination angle θ generally facilitates particle flow and accumulation. This assumption proved effective in our study. Nevertheless, for more complex flow behaviors, it is recommended that future studies derive an explicit sensitivity expression of the objective function with respect to θ for the entire optimization framework, serving as a mathematically rigorous alternative to the current heuristic strategy.

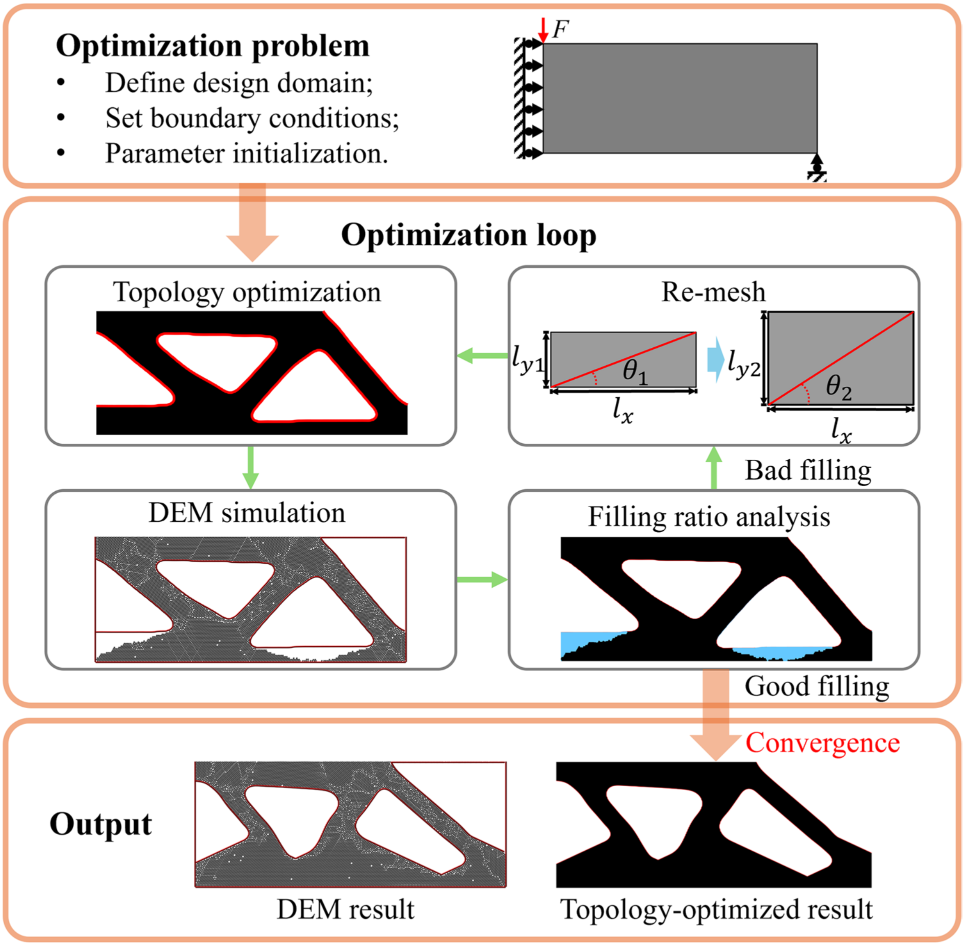

Fig. 12 Illustration of the optimization framework

Table 1 Parameters initialization in topology optimization (TO)

TO Parameters	Value	Equation No
Filtering radius	$r_{\min}=12$	(12)
Projection threshold	$\eta=0.2$	(13)
Poisson's ratio of elements	$v=0.3$	(15)
Young's modulus of elements	$E_0=1$; $E_{\min}=10^{-9}$	(16)

Table 2 Physical and contact parameters in DEM simulations

DEM Parameters	Value	Equation No
Time step	$\Delta t=0.001$ s	(18),(19)
Surface energy	$\gamma=5$	(20),(23)
Young's modulus of particles	$E_{\mathrm{I,II}}=2\times10^7$ Pa	(21)
Poisson's ratio of particles	$v_{\mathrm{I,II}}=0.3$	(21),(26)
Particle radius	$R_{\mathrm{I,II}}=5$ mm	(22)
Friction coefficient	$\mu=0.1$	(27)
Density of particles	$m_{\mathrm{I,II}}=2400$ kg/m^3	(30)

3 Numerical studies

This section illustrates the effectiveness of the proposed topology optimization framework through different examples. The following parameters are selected and remain consistent across all examples.

For the topology optimization module, the essential initialization parameters are listed in Table 1. To facilitate reference, the corresponding equation numbers are provided in the last column of the Table. A continuous scheme is employed for a better convergence: (i) The volume constraint fraction f in Eq. (14) is initially set to 99% and decreases by 2% every 10 iterations until the target volume fraction is reached; (ii) Upon reaching the target volume fraction, the sharpness parameter β in Eq. (13) starts from 5 and doubled every 25 iterations until it reaches 40. The iterative process is considered converged when the normalized Euclidean norm between two successive iterations of the design variable $\mathbf{x}$ falls below 10^{-6}, or when the maximum number of 400 iterations is reached.

The parameters for the DEM simulation module are provided in Table 2. To facilitate the analysis and comparison of the filling ratio, the total DEM simulation time is set to 10 s for all examples, and the time step is defined as $\Delta t=0.001$ s.

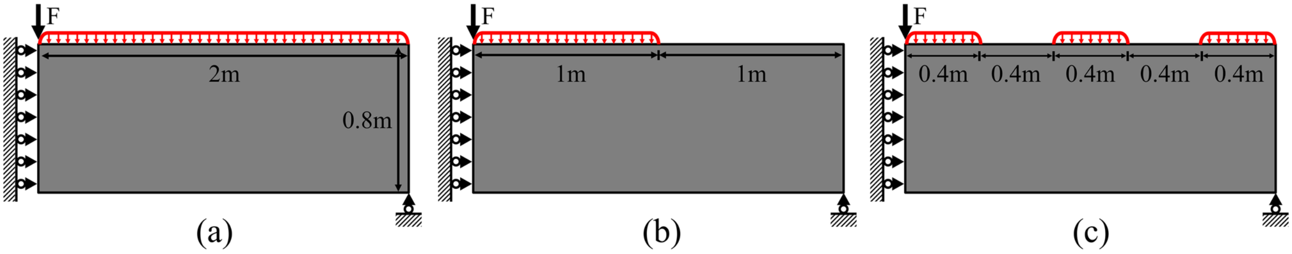

Fig. 13 Design domain, boundary conditions, and casting positions (indicated in red arrow) for MBB beam problems

All particles are modeled as spherical with uniform radius. In the casting process, the initial velocity of all particles is set to 0 m/s. They are subsequently subjected to gravitational acceleration (9.81 m/s^2) and allowed to settle freely until the total DEM simulation time is reached. It is important to note that the parameters selected here serve as an example to validate the proposed optimization framework and can be adjusted according to specific engineering requirements.

The convergence criterion of the entire optimization framework is stipulated as the identified filling ratio being more than 99.5%, expressed as $FR \geq 99.5\%$ in Eq. (32).

3.1 Messerschmitt-Bölkow-Blohm beam

The first example is the Messerschmitt-Bölkow-Blohm (MBB) beams, where three different casting opening cases are predefined, as shown in Fig. 13. Due to symmetry, only half of the design domain is considered in the optimization, which is discretized using 4-node rectangular elements with 300 elements in the horizontal direction. The number of elements in the vertical direction depends on the aspect ratio (l_y/l_x) of the rectangular elements, which is related to the angle of repose θ. A unit point load is applied at the top-left of the beam. The prescribed volume fraction is 55%.

Figure 14 demonstrates the results of topology optimization, DEM simulation, and filling ratio identification for three casting cases, along with a comparison of the results obtained using the conventional optimization method. When the entire top surface is designated as the casting position, the optimization converges at an angle of 30°, with a final filling ratio of 99.83% (Fig. 14a). In comparison, the benchmark structure achieved a filling ratio of 95.56% under the same casting condition, with 4.44% of the void regions primarily located in the tensile zones (i.e., bottom region). This improper filling increases the risk of tensile failure in the beam.

The problem of improper filling becomes more serious when the casting opening is limited to only half of the designated region, as shown in Fig. 14b. The filling ratio of the benchmark design is only 67.23%, with the entire right side of the structure almost hollow. In contrast, the beam obtained using the proposed optimization framework yields a filling ratio of 99.88%, with an inclined angle of 35°.

Additionally, the configuration of multiple casting openings is investigated. Figure 14c illustrates the case where three casting openings are predefined at the top during optimization. The proposed optimization framework increased the filling ratio from 92.48% to 99.86% compared to the benchmark design. Moreover, the results indicate that although three casting openings were predefined, the rightmost one proved to be redundant. This is because the region at the top right corner is less sensitive to compliance and is preferentially eliminated in the optimization process.

The compliance of the entire structure (C) and the infilled structure ($\overline{C}$) are presented at the bottom of each image in Fig. 14. A quantitative summarization is listed in Table 3. It reveals that the proposed optimization framework leads to a 10–20% increase in the normalized compliance C of the entire structure. This is a common outcome in multi-constraint problems, and the optimized structure may deviate from the initial compliance-optimal design when additional constraints are introduced, leading to an observable increase in compliance. Sometimes, it is not excluded that additional constraints could reduce compliance, since the benchmark structure obtained for the large-scale non-convex optimization problem is a locally optimal design (Rozvany 2009). However, designs exhibit the normalized compliance $\overline{C}$ superior to (i.e., lower than) the benchmark design for the infilled structure, especially for the case-b. A structure holds value only if it can be conveniently manufactured and utilized, and sacrificing a small degree of performance to enhance manufacturability is often encouraged. This trade-off between performance and manufacturability is particularly important in engineering applications.

The iterative results of the optimization process are summarized in Appendix D. Notably, a larger θ does not necessarily result in a higher filling ratio. For instance, the void ratio of case-a observed at $\theta = 20°$ is greater than that at $\theta = 15°$. This phenomenon highlights the inherent complexity of the material filling process, which is influenced by the intricate interactions between particles and the geometry of the formwork. These interactions, governed by particle flow dynamics and geometric constraints, result in nonlinear

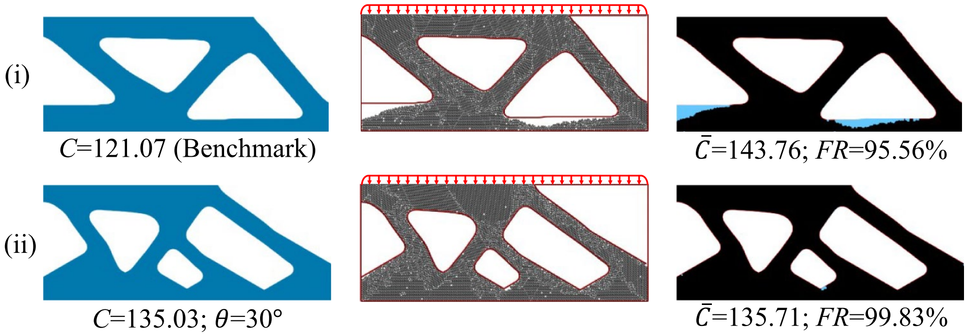

(a) Results for MBB beam with a full opening at the top.

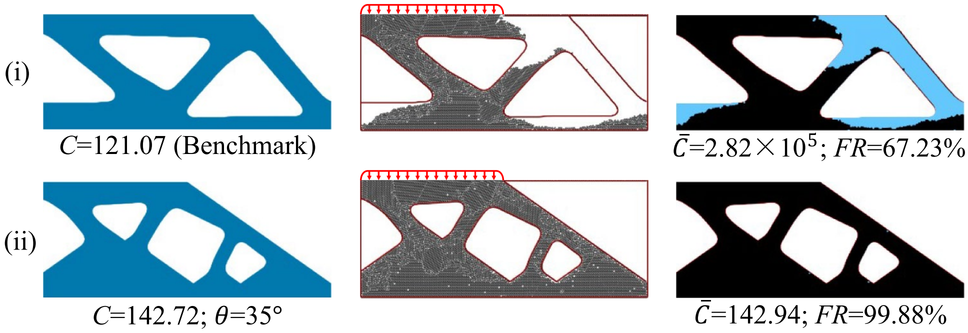

(b) Results for MBB beam with a half opening at the top left.

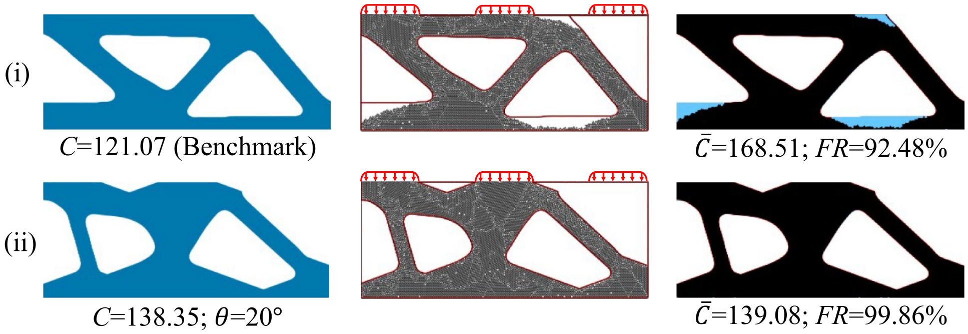

(c) Results for MBB beam with three openings at the top.

Fig. 14 Comparison of results for MBB beam with different opening types at the top, obtained using (i) conventional method and (ii) proposed optimization framework: (left) optimized results, (middle) DEM simulation, and (right) filling ratio identification

Table 3 A comparison analysis of MBB beam results

Opening	Angle (θ)	Filling ratio (FR)/Void ratio (1-FR)	Compliance	
			Normalized C	Normalized $\bar{C}$
Case-a	Benchmark	95.56% (4.44%)	100%	100%
	30°	99.83% (0.17%)	111.53% ↑	94.40% ↓
Case-b	Benchmark	67.23% (32.77%)	100%	100%
	35°	99.88% (0.12%)	117.88% ↑	0.05% ↓
Case-c	Benchmark	92.48% (7.52%)	100%	100%
	20°	99.86% (0.14%)	114.27% ↑	82.54% ↓

behaviors within the DEM simulation process (Mechtcherine et al. 2014; Zhang et al. 2020). Fortunately, the void ratio exhibits an overall decreasing trend, which validates the effectiveness of the proposed optimization framework and the geometric characteristics discussed in Sect. 2.1.

3.2 Cantilever beam

The second numerical example is a cantilever beam with three casting cases. The boundary conditions and openings are illustrated in Fig. 15. The design domain is discretized into 4-node rectangular elements, with 300 elements distributed along the horizontal axis to ensure adequate resolution for the optimization process. A unit point load is applied at the bottom-right corner of the design domain, with a prescribed volume fraction of 55%.

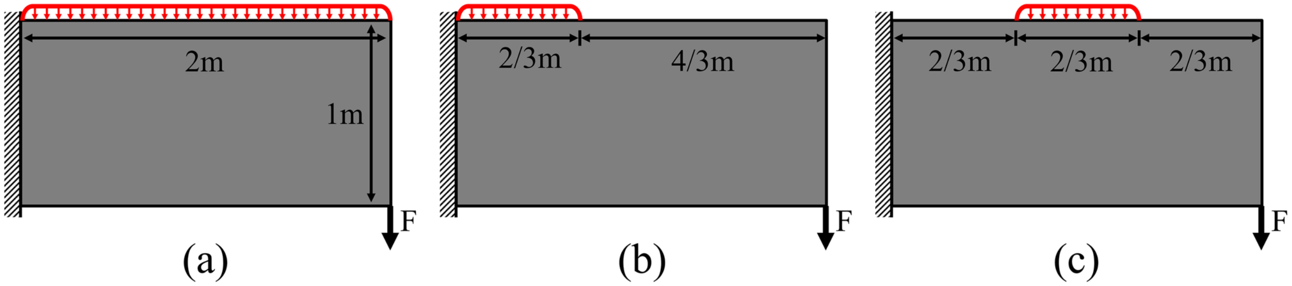

Fig. 15 Design domain, boundary conditions, and casting positions (indicated in red arrow) for cantilever beam problems

Figure 16 displays three topology-optimized results with different casting openings. Comparing the three benchmark designs, it is obvious that the bottom region remains the most challenging area to fill. Moreover, significant variations in filling efficiency are observed with the reduction of the casting opening size and changes in casting positions. Generally, the highest filling ratio of 96.86% is achieved when the top is fully open. However, the filling ratio declines as the casting opening decreases and its position shifts. For instance, the filling ratio drops to only 67.96% when the opening is positioned on the left side (Fig. 16b). Under the prescribed boundary conditions, the bottom of the beam experiences compressive stress, and improper filling in this region increases the risk of structural failure due to compression.

The proposed optimization framework accounts for the influence of casting positions, resulting in all three topology-optimized designs achieving a filling ratio of over 99.5%. Similarly, the entire structure's compliance exceeds the benchmark design. As shown in Table 4, normalized compliance C increases by 4.78% when the top is fully open. When the casting opening is located in the middle, compliance rises significantly by 28.92%. This substantial increase is attributed to the suppression of material generation near the fixed boundary in the upper-left region, which compromises the performance of the tensile zone. Therefore, it can be concluded that the position of the casting opening is recommended to be reasonably initialized based on practical experience during optimization to minimize the loss of structural performance. It should be highlighted that the compliance of the infilled structures ($\overline{C}$) is lower than that of the infilled benchmark structures, indicating that structural integrity could have a significant impact on performance.

3.3 Walls

Figure 17 presents the third numerical example, featuring walls subjected to different boundaries and passive void domains (i.e., non-optimized void domains). A resolution of 300 rectangular elements is adopted in the horizontal direction for the design domain. A uniformly distributed load of two units per meter is applied along the wall's top and bottom edges. The casting opening is defined as the entire top surface due to the load applied to the whole top surface. The problems are optimized using a total volume fraction of 45%.

Figure 18a demonstrates the results under the boundary condition of case-a. As summarized in Table 5, a void region accounting for 13.80% is observed in the central bottom area of the wall in the benchmark design. Employing the proposed optimization framework, the topology-optimized result converges at a 15° angle with a filling ratio of 99.72%. Comparing the two designs, it is evident that the bottom region undergoes a significant geometric transformation, exhibiting a distinct inclination. This inclined topology is advantageous for improving the casting and filling efficiency. Figure 18b shows the results under the boundary condition of case-b, where two passive void domains are prescribed in this case. Similar to case-a, the bottom region exhibits casting challenges, with a void ratio of 3.10%. However, the design obtained using the proposed optimization framework yields a design converging at 15°, significantly improving the geometry of the bottom region and reducing the void ratio to 0.28%.

The compliance of the entire solid designs of case-a and case-b is 105.39 and 43.03, respectively, representing an increase of 25.79% and 11.05% compared to their benchmark designs (Table 5). Notwithstanding, by comparing the compliance of the infilled structure ($\overline{C}$), the mechanical properties of the structure with a high filling ratio are better than those of the benchmark structure with a low filling ratio. The designs optimized by the proposed method effectively balance manufacturing constraints and mechanical performance, making them favorable choices for practical implementation.

4 Experimental tests

This section presents a simple casting experiment on an MBB beam (Fig. 14 case-a) to validate the effectiveness of the proposed method. A 1:8 scaled-down formwork

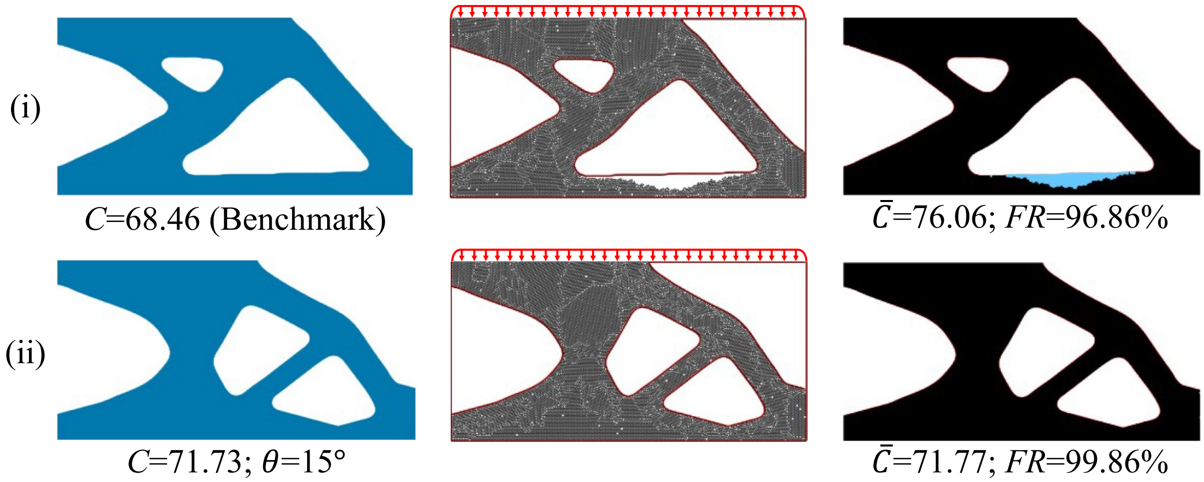

(a) Results for cantilever beam with a full opening at the top.

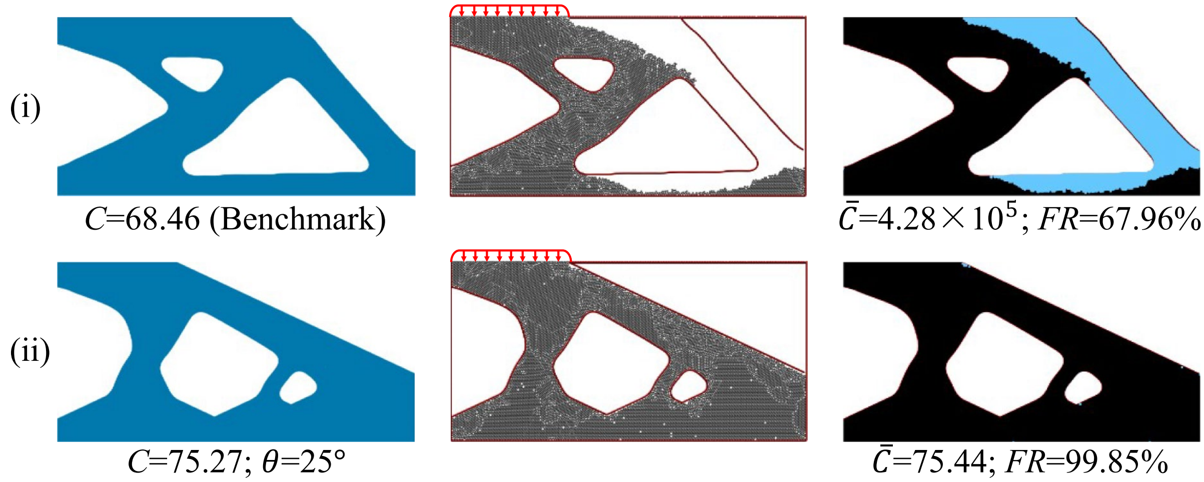

(b) Results for cantilever beam with a 1/3 opening at the top left.

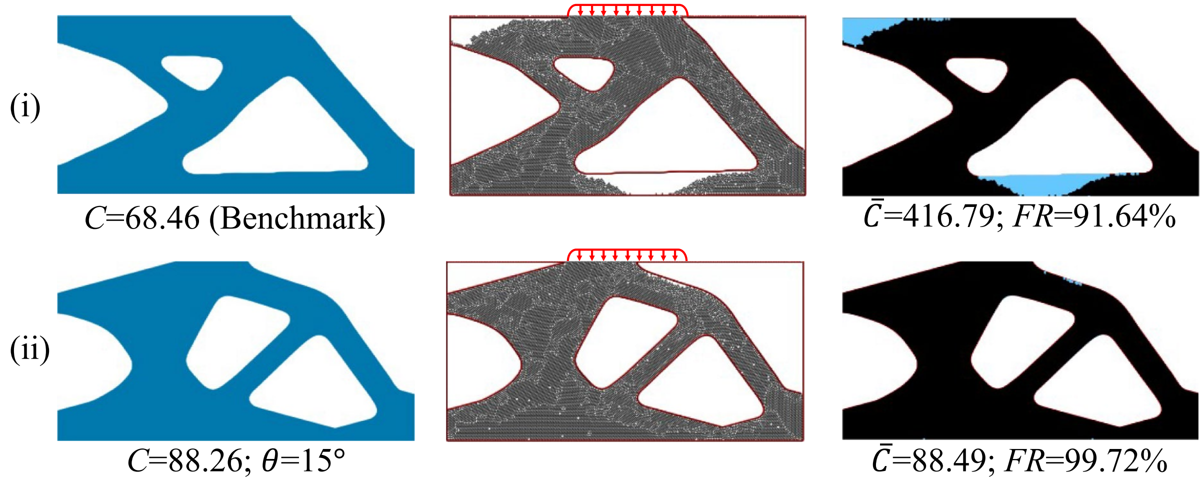

(c) Results for cantilever beam with a 1/3 opening at the top middle.

Fig. 16 Comparison of results for cantilever beam with different opening types at the top, obtained using (i) conventional method and (ii) proposed optimization framework: (left) optimized results, (middle) DEM simulation, and (right) filling ratio identification

Table 4 A comparison analysis of cantilever beam results

Opening	Angle (θ)	Filling ratio (FR)/Void ratio (1-FR)	Compliance	
			Normalized C	Normalized $\overline{C}$
Case-a	Benchmark	96.86% (3.14%)	100%	100%
	15°	99.86% (0.14%)	104.78% ↑	94.36% ↓
Case-b	Benchmark	67.96% (32.04%)	100%	100%
	25°	99.85% (0.15%)	109.95% ↑	0.02% ↓
Case-c	Benchmark	91.64% (8.36%)	100%	100%
	15°	99.72% (0.28%)	128.92% ↑	21.23% ↓

is fabricated using fused filament fabrication (FFF), as shown in Fig. 19. The formwork dimensions are defined as 500 mm × 100 mm × 30 mm. One side of the formwork is made of a transparent plate, allowing for the observation of the concrete's filling state. The OPTIMIX BP138 (i.e., cement-fine aggregate modified mixture) is utilized with a water-to-mixture ratio of 0.26:1.

It should be noted that the parameter testing of the mixed concrete materials exceeds the scope of this study. The experiment conducted here is a simple comparative test of the effectiveness of casting in formwork with the same material. The concrete material is cast from the top through a funnel, flowing and filling under gravity. Figure 20 illustrates the filling state of both the benchmark formwork and the formwork optimized by the proposed method. It can be observed that unfilled zones appear at the bottom of the benchmark formwork, as illustrated in the detailed views in Fig. 20c. Since this is a scaled-down experiment and the parameters of the mixed materials have not been tested, the final filling state may differ from the DEM simulation. However, the optimized formwork achieves good filling, indicating the effectiveness of the proposed approach. The casting video can be found in the supplementary material.

5 Extension to 3D

The extension of the optimization framework from 2D to 3D is straightforward. This section demonstrates the 3D topology optimization to showcase the generalizability of the proposed method. The 8-node hexahedral elements are used in 3D, and the smoothing filter in Eq. (10) is applied within a spherical radius $r_{\min}$ (Fig. 21a). The casting filter depends on the maximum density among the five upper neighboring elements, highlighted in black in Fig. 21b. Therefore, Eqs. (4) and (5) can be extended to 3D as follows:

$$\rho_{c(i,j,w)} = \min\left(\rho_{(i,j,w)}, \rho_{b(i,j,w)}\right) \tag{33}$$

$$\begin{aligned}\rho_{b(i,j,w)} &= \\ &\max\left(\rho_{c(i-1,j-1,w)}, \rho_{c(i,j-1,w)}, \rho_{c(i+1,j-1,w)}, \rho_{c(i,j-1,w-1)}, \rho_{c(i,j-1,w+1)}\right)\end{aligned} \tag{34}$$

Figure 22 illustrates a 3D MBB beam problem featuring a fully open casting inlet at the top. The design domain is discretized as 120 × 24 elements in the xz-plane, with the y-direction resolution determined by the angle (θ). A uniformly distributed load of 1 unit per length L is applied at the beam's midspan. The problems are solved with a volume fraction of 30%, a filter radius of $r_{\min} = 4$, and a threshold parameter of $\eta = 0.4$ for the robust formulation; other parameters follow the 2D settings. Two prescribed angles ($\theta = 30°$ and $\theta = 45°$) are tested.

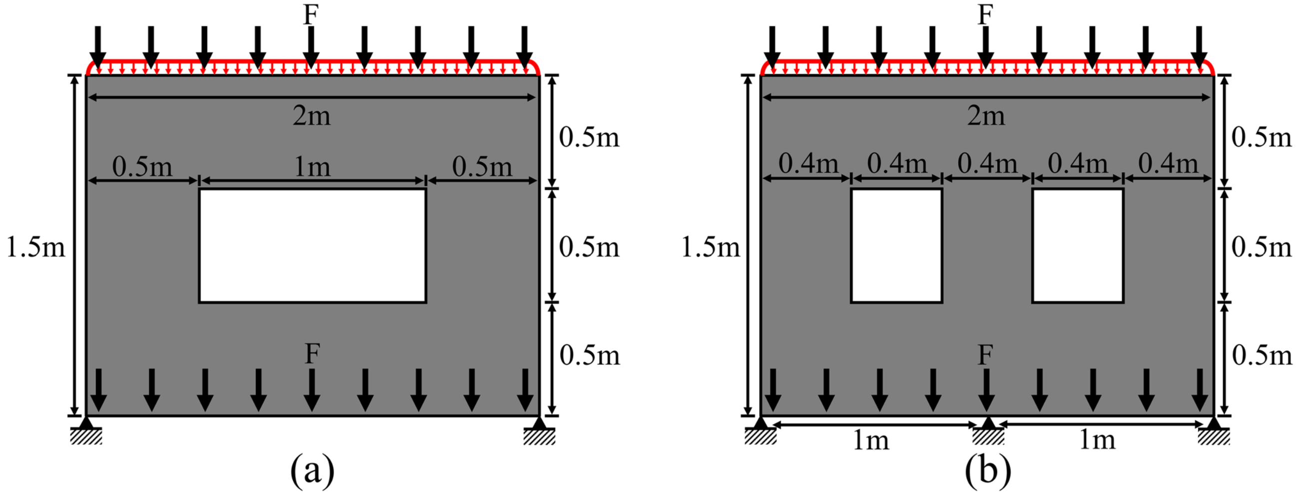

Fig. 17 Design domain, boundary conditions, and casting positions (indicated in red arrow) for wall problems

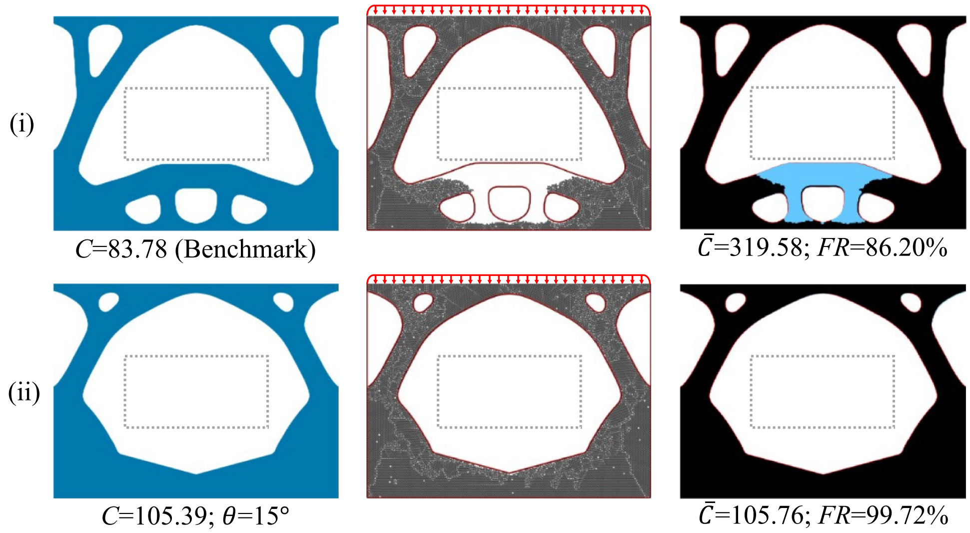

(a) Results for wall with *boundary condition-(a)*.

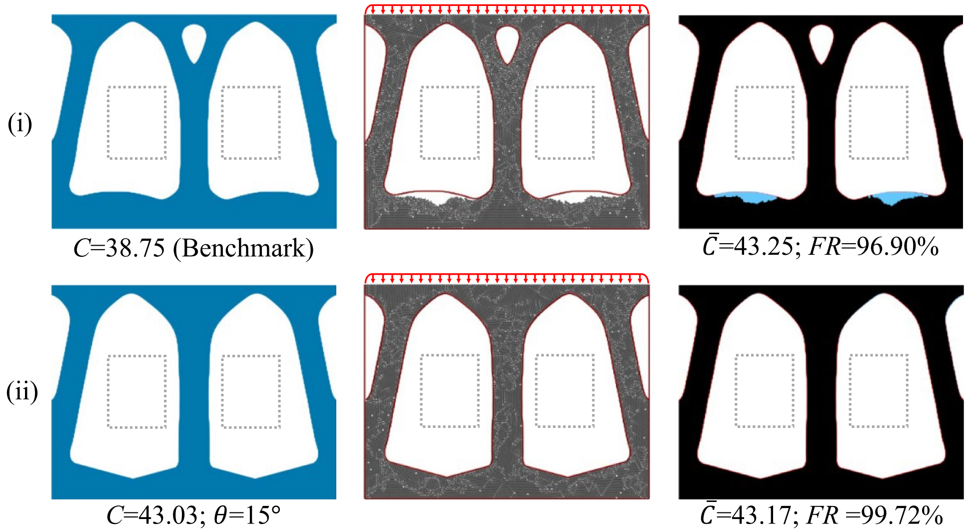

(b) Results for wall with *boundary condition-(b)*.

Fig. 18 Comparison of results for walls with a full opening at the top under different boundary conditions and passive domains, obtained using (i) conventional method and (ii) proposed optimization framework: (left) optimized results, (middle) DEM simulation, and (right) filling ratio identification

Table 5 A comparison analysis of wall results

Problem	Angle (θ)	Filling ratio (FR)/Void ratio (1-FR)	Compliance	
			Normalized C	Normalized $\bar{C}$
Case-a	Benchmark	86.20% (13.80%)	100%	100%
	15°	99.72% (0.28%)	125.79% ↑	33.09% ↓
Case-b	Benchmark	96.90% (3.10%)	100%	100%
	15°	99.72% (0.28%)	111.05% ↑	99.82% ↓

The optimized results are shown in Fig. 24b, where different prescribed angles yield varying surface inclination patterns. However, it is worth noting that the results in Fig. 24b omit structural connectivity. For 3D structure casting, ensuring connectivity is essential to prevent enclosed cavities and guarantee manufacturability (Tong et al. 2025). Incorporating connectivity constraints is a direct way to address this issue. This study also conducts a preliminary exploration to demonstrate the compatibility of the topology optimization module with additional constraints. A "complementary approach" is employed after the projected density field in this work to guarantee structural connectivity, as illustrated in Fig. 23. Full details are available in the authors' previous work (Tong et al. 2025).

Figure 24c presents the optimized results with the connectivity constraint, which effectively eliminates internal

Fig. 19 Formwork design of MBB beam generated by (**a**) conventional method and (**b**) proposed optimization framework

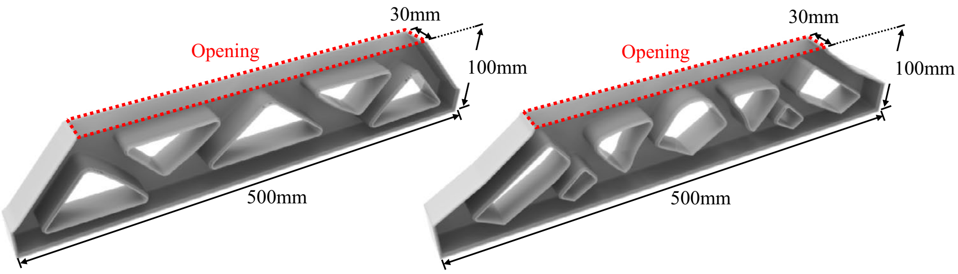

(a) (b)

Fig. 20 3D printed formwork and filling state of MBB beam: **a** benchmark design, and **b** design with proposed method; (**c**) Detailed views of improperly filled zones

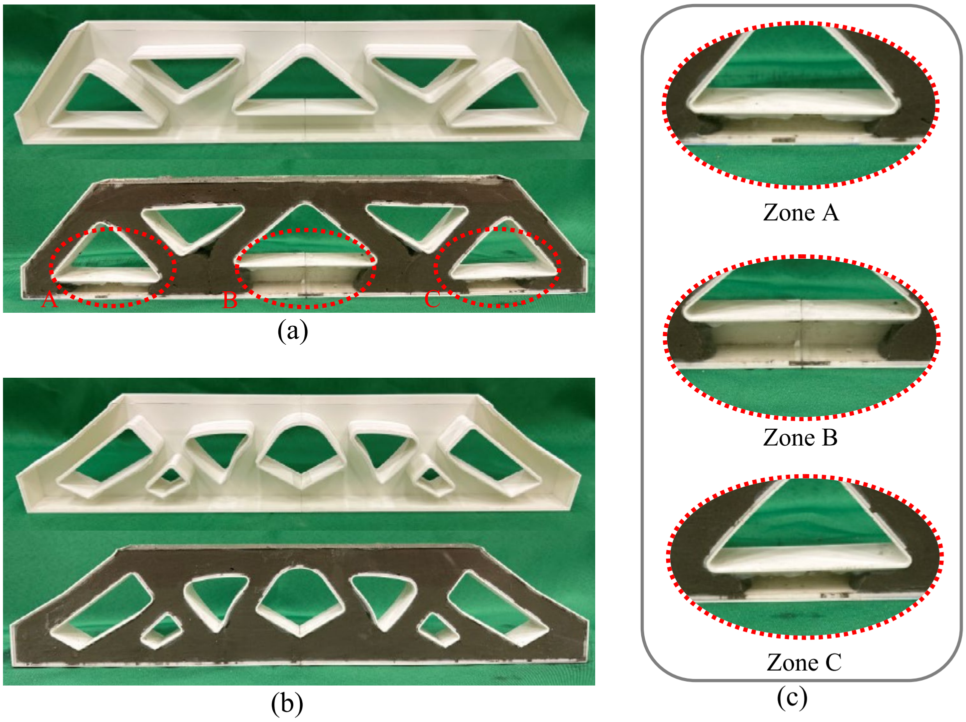

(a)

(b)

(c)

Fig. 21 **a** Smoothing filter for hexahedral elements; **b** Casting filter with process-dependent material migration process in 3D

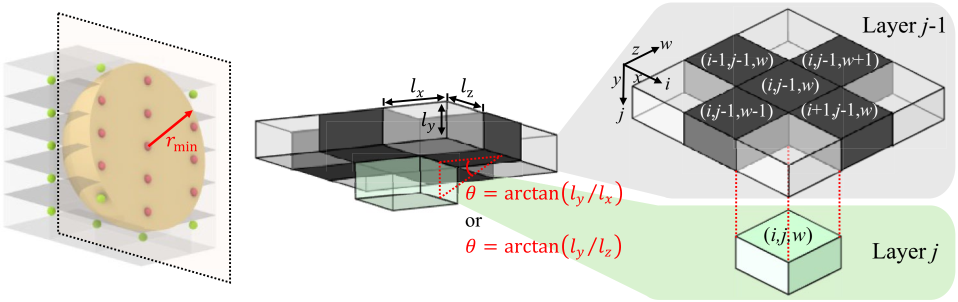

(a) (b)

enclosed cavities in all structures. Quantitatively, some optimized structures achieve better (i.e., lower) compliance than the benchmark, which indicates that the benchmark design is a local optimum for this non-convex optimization problem. Furthermore, comparing the designs in Fig. 24b and c, it is found that the "complementary approach" has the potential to simplify geometric complexity and alleviate manufacturing difficulties.

The 3D example demonstrates the flexibility and compatibility of the topology optimization module. Future work could continue to consider extending the DEM simulation part into 3D to refine the 3D optimization

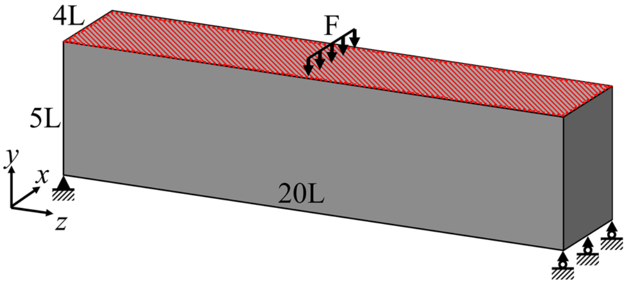

Fig. 22 Design domain, boundary conditions, and casting positions (indicated in red region) for 3D MBB beam problems

framework. Moreover, additional manufacturing constraints can be incorporated into the 3D topology optimization module as needed, such as introducing demoldable constraints for formwork design (Sato et al. 2017; Wang et al. 2020a) to facilitate fabrication and enable reusability. This represents a promising direction for future research; however, it is beyond the scope of this study.

6 Conclusion

This study presents a process simulation-informed topology optimization framework that incorporates geometric constraints imposed by the casting process, providing improved structure and formwork design solutions. A four-field scheme is employed to control the inclined angle and length scale of the geometrical shape. The proposed optimization framework ensures that topology-optimized structures are compatible with casting processes, minimizing the risk of large unfilled voids and enhancing the overall structural integrity. Additionally, this method enables the flexible customization of casting positions of the

Fig. 23 Illustration of optimization scheme considering connectivity constraints

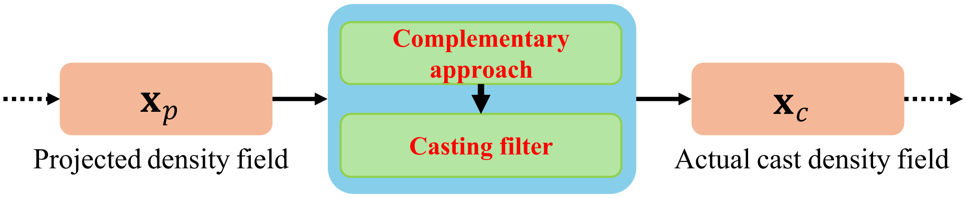

Fig. 24 **a** Benchmark design; **b** and **c** Designs without and with connectivity constraint for 30° and 45° angles. The casting positions are highlighted in red

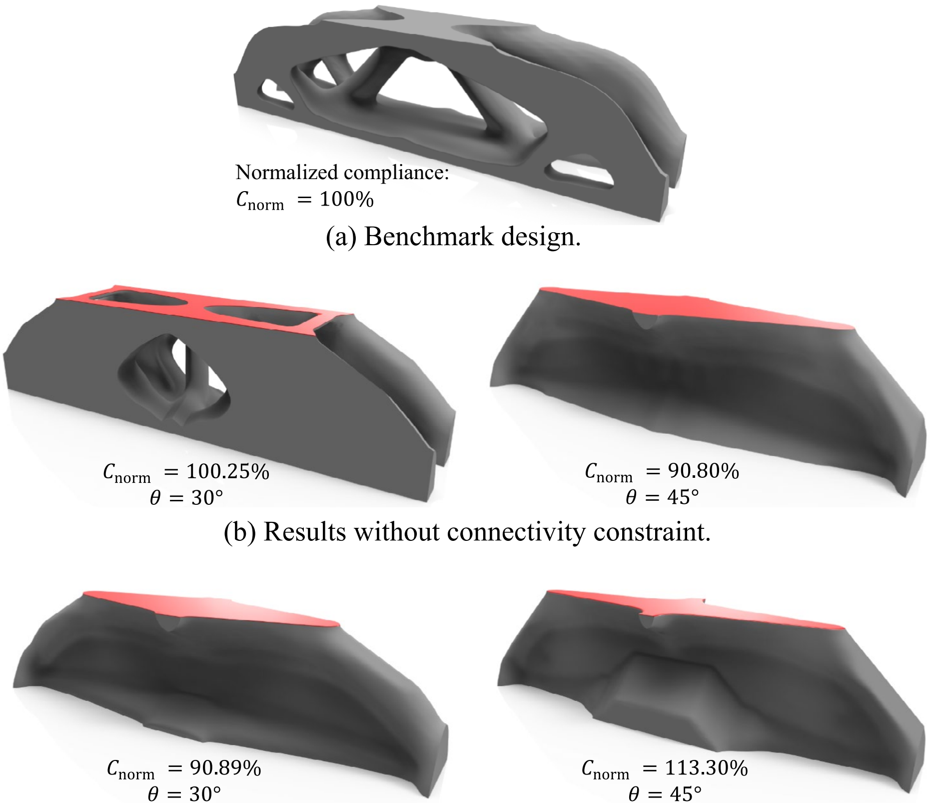

(a) Benchmark design.

(b) Results without connectivity constraint.

(c) Results with connectivity constraint.

formwork, offering greater adaptability to specific design requirements.

The effectiveness of the proposed optimization framework has been verified by three numerical examples. The results reveal that the filling ratios have improved, resulting in the compliance of the infilled structures being preferable to the benchmark designs. Furthermore, an experimental test is provided to verify that the proposed optimized formwork achieves improved filling efficiency compared to the benchmark designs. This trade-off between minor performance losses and significant improvements in manufacturability underscores the practical value of the framework. The extension of the optimization framework from 2D to 3D has also been initiated in this study and will be further developed in future work.

It should be noted that material flow is a complex research discipline; this work considers only two geometric characteristics (i.e., angle and length scale), and other factors may also influence casting. Future work could explore incorporating coupled factors to enhance the generalizability of the optimization framework, such as aggregate shape. Furthermore, the current implementation assumes a structured voxel-based discretization. While this enables efficient filtering, it may limit geometric fidelity in cases involving curved or complex boundaries. Future extensions of this framework could incorporate unstructured meshes (Wu 2018; Zhuang et al. 2024b) with manufacturing constraints, thereby enabling a more effective treatment of complex design domains. Overall, by ensuring enhanced casting efficiency and addressing manufacturability constraints, the proposed method facilitates the broader adoption of topology-optimized structures in real-world engineering applications.

Appendix A

Element stiffness matrix

$$\mathbf{k}_0 = \int_{\Omega} \mathbf{B}^{\top}\mathbf{D}\mathbf{B}\mathrm{d}\Omega \tag{35}$$

For 4-node rectangular elements, the strain–displacement matrix (**B**) and elasticity matrix (**D**) have:

$$\mathbf{B} = \begin{bmatrix} \mathbf{B}_1 & \mathbf{B}_2 & \mathbf{B}_3 & \mathbf{B}_4 \end{bmatrix} \tag{36}$$

$$\mathbf{B}_{\varsigma} = \begin{bmatrix} \frac{\partial N_{\varsigma}}{\partial x} & 0 \\ 0 & \frac{\partial N_{\varsigma}}{\partial y} \\ \frac{\partial N_{\varsigma}}{\partial y} & \frac{\partial N_{\varsigma}}{\partial x} \end{bmatrix}; (\varsigma = 1, 2, 3, 4) \tag{37}$$

$$\mathbf{D} = \frac{E}{1 - \nu^2}\begin{bmatrix} 1 & \nu & 0 \\ \nu & 1 & 0 \\ 0 & 0 & (1 - \nu^2)/2 \end{bmatrix} \tag{38}$$

where N_{ς} is the shape function (also known as nodal interpolation function) of elements, E is the elastic modulus, and ν is the Poisson's ratio.

Appendix B

Sensitivity analysis and verification

- Sensitivity analysis

The sensitivity analysis of the four-field scheme can be determined by the chain rule as follows:

$$\frac{\partial \varphi}{\partial \mathbf{x}} = \frac{\partial \mathbf{x}_s}{\partial \mathbf{x}}\frac{\partial \mathbf{x}_p}{\partial \mathbf{x}_s}\frac{\partial \mathbf{x}_c}{\partial \mathbf{x}_p}\frac{\partial \varphi}{\partial \mathbf{x}_c} \tag{39}$$

where φ represents the objective function C or volume constraint function V in Eq. (14). The detailed sensitivities are elaborated in the following paragraphs.

(1) $\partial C/\partial \mathbf{x}_c$ and $\partial V/\partial \mathbf{x}_c$

The sensitivity of the compliance function C can be driven by the adjoint method:

$$\begin{aligned} \frac{\partial C}{\partial x_{c(i,j)}} = -\mathbf{U}^{\top}\frac{\partial \mathbf{K}}{\partial x_{c(i,j)}}\mathbf{U} = -P\left(x_{c(i,j)}\right)^{P-1}\left(E_0 - E_{\min}\right) \\ \mathbf{u}_{c(i,j)}^{\top}\mathbf{k}_0\mathbf{u}_{c(i,j)}; \left(x_{c(i,j)} \in \mathbf{x}_c\right) \end{aligned} \tag{40}$$

where the footnote (i,j) represents the index of element (i,j) in the actual cast density matrix $\mathbf{x}_c$, $\mathbf{u}_{c(i,j)}$ is the element displacement vector. Similarly, the sensitivity of the volume constraint function is:

$$\frac{\partial V}{\partial x_{c(i,j)}} = 1; \left(x_{c(i,j)} \in \mathbf{x}_c\right) \tag{41}$$

(2) $\partial \varphi/\partial \mathbf{x}_p$

$$\frac{\partial \varphi}{\partial \mathbf{x}_p} = \frac{\partial \mathbf{x}_c}{\partial \mathbf{x}_p}\frac{\partial \varphi}{\partial \mathbf{x}_c} \tag{42}$$

In Eq. (39), it is obvious that the sensitivity of $\partial\mathbf{x}_c/\partial\mathbf{x}_p$ needs to be computed. However, as mentioned in Sect. 2.2.1, the actual cast density ($\mathbf{x}_c$) of layer i depends on the projected density ($\mathbf{x}_p$) of layer i-1. Direct calculation of $\partial\mathbf{x}_c/\partial\mathbf{x}_p$ is computationally expensive; therefore, the adjoint method is employed here to calculate $\partial\varphi/\partial\mathbf{x}_p$ rather than $\partial\mathbf{x}_c/\partial\mathbf{x}_p$. A detailed derivation is provided below.

The actual cast density in layer i ($\mathbf{x}_{c,i}$) can be written as a function in terms of projected density in layer i ($\mathbf{x}_{p,i}$) and actual cast density in layer i-1 ($\mathbf{x}_{c,i\text{-}1}$), which is:

$$\mathbf{x}_{c,i} = \mathbf{f}\left(\mathbf{x}_{p,i}, \mathbf{x}_{c,i-1}\right) = \mathbf{f}_{c,i} \tag{43}$$

By employing the adjoint method, the function φ is expressed as:

$$\varphi = \hat{\varphi} = \varphi(\mathbf{x}_c) + \sum_{i=1}^{n_y} \boldsymbol{\lambda}_i^{\top}\left(\mathbf{f}_{c,i} - \mathbf{x}_{c,i}\right) \tag{44}$$

Differentiation of Eq. (44) gives:

$$\frac{\partial \varphi}{\partial \mathbf{x}_{p,k}} = \frac{\partial \hat{\varphi}}{\partial \mathbf{x}_{p,k}} = \sum_{i=1}^{n_y}\left[\frac{\partial \mathbf{x}_{c,i}}{\partial \mathbf{x}_{p,k}}\frac{\partial \varphi}{\partial \mathbf{x}_{c,i}} + \left(\delta_{ik}\mathbf{I}\frac{\partial \mathbf{f}_{c,i}}{\partial \mathbf{x}_{p,i}} + \frac{\partial \mathbf{x}_{c,i-1}}{\partial \mathbf{x}_{p,k}}\frac{\partial \mathbf{f}_{c,i}}{\partial \mathbf{x}_{c,i-1}} - \frac{\partial \mathbf{x}_{c,i}}{\partial \mathbf{x}_{p,k}}\right)\boldsymbol{\lambda}_i\right] \tag{45}$$

where n_y is the total number of layers, i and k are the layer indexes, respectively. δ_{ik} is the Kronecker delta ($i=k$, $\delta_{ik}=1$; $i\neq k$, $\delta_{ik}=0$). Since $\mathbf{x}_{c,i}$ only depends on the density in layer i and i-1, $\partial\mathbf{x}_{c,i}/\partial\mathbf{x}_{p,k}=\mathbf{0}$ for $k>i$. Therefore, Eq. (45) can be simplified as:

$$\frac{\partial \varphi}{\partial \mathbf{x}_{p,k}} = \frac{\partial \mathbf{x}_{c,k}}{\partial \mathbf{x}_{p,k}}\frac{\partial \varphi}{\partial \mathbf{x}_{c,k}} + \sum_{i=k+1}^{n_y}\left[\frac{\partial \mathbf{x}_{c,i}}{\partial \mathbf{x}_{p,k}}\left(\frac{\partial \varphi}{\partial \mathbf{x}_{c,i}} - \boldsymbol{\lambda}_i\right) + \frac{\partial \mathbf{x}_{c,i-1}}{\partial \mathbf{x}_{p,k}}\frac{\partial \mathbf{f}_{c,i}}{\partial \mathbf{x}_{c,i-1}}\boldsymbol{\lambda}_i\right] \tag{46}$$

Eq. (46) can be expanded as:

$$\begin{aligned}\frac{\partial \varphi}{\partial \mathbf{x}_{p,k}} &= \frac{\partial \mathbf{x}_{c,k}}{\partial \mathbf{x}_{p,k}}\frac{\partial \varphi}{\partial \mathbf{x}_{c,k}} + \sum_{i=k+1}^{n_y}\frac{\partial \mathbf{x}_{c,i}}{\partial \mathbf{x}_{p,k}}\left(\frac{\partial \varphi}{\partial \mathbf{x}_{c,i}} - \boldsymbol{\lambda}_i\right)\\ &+\frac{\partial \mathbf{x}_{c,k}}{\partial \mathbf{x}_{p,k}}\frac{\partial \mathbf{f}_{c,k+1}}{\partial \mathbf{x}_{c,k}}\boldsymbol{\lambda}_{k+1} + \sum_{i=k+2}^{n_y}\frac{\partial \mathbf{x}_{c,i-1}}{\partial \mathbf{x}_{p,k}}\frac{\partial \mathbf{f}_{c,i}}{\partial \mathbf{x}_{c,i-1}}\boldsymbol{\lambda}_i\end{aligned} \tag{47}$$

Re-adjust the summation indexes of the last term, it has:

$$\sum_{i=k+2}^{n_y}\frac{\partial \mathbf{x}_{c,i-1}}{\partial \mathbf{x}_{p,k}}\frac{\partial \mathbf{f}_{c,i}}{\partial \mathbf{x}_{c,i-1}}\boldsymbol{\lambda}_i = \sum_{i=k+1}^{n_y-1}\frac{\partial \mathbf{x}_{c,i}}{\partial \mathbf{x}_{p,k}}\frac{\partial \mathbf{f}_{c,i+1}}{\partial \mathbf{x}_{c,i}}\boldsymbol{\lambda}_{i+1} \tag{48}$$

Consequently, Eq. (47) can be rewritten as:

$$\begin{aligned}\frac{\partial \varphi}{\partial \mathbf{x}_{p,k}} &= \frac{\partial \mathbf{x}_{c,k}}{\partial \mathbf{x}_{p,k}}\left(\frac{\partial \varphi}{\partial \mathbf{x}_{c,k}} + \frac{\partial \mathbf{f}_{c,k+1}}{\partial \mathbf{x}_{c,k}}\boldsymbol{\lambda}_{k+1}\right) + \frac{\partial \mathbf{x}_{c,n_y}}{\partial \mathbf{x}_{p,k}}\left(\frac{\partial \varphi}{\partial \mathbf{x}_{c,n_y}} - \boldsymbol{\lambda}_{n_y}\right)\\ &+ \sum_{i=k+1}^{n_y-1}\frac{\partial \mathbf{x}_{c,i}}{\partial \mathbf{x}_{p,k}}\left(\frac{\partial \varphi}{\partial \mathbf{x}_{c,i}} - \boldsymbol{\lambda}_i + \frac{\partial \mathbf{f}_{c,i+1}}{\partial \mathbf{x}_{c,i}}\boldsymbol{\lambda}_{i+1}\right)\end{aligned} \tag{49}$$

Since $\mathbf{x}_c=\mathbf{f}_c$ (Eq. (43)) and the Lagrange multipliers can be chosen arbitrarily, the following multipliers are defined:

$$\begin{cases}\boldsymbol{\lambda}_i = \dfrac{\partial \varphi}{\partial \mathbf{x}_{c,i}} + \dfrac{\partial \mathbf{x}_{c,i+1}}{\partial \mathbf{x}_{c,i}}\boldsymbol{\lambda}_{i+1};(1 \le i < n_y)\\ \boldsymbol{\lambda}_{n_y} = \dfrac{\partial \varphi}{\partial \mathbf{x}_{c,n_y}};(i = n_y)\end{cases} \tag{50}$$

Therefore, Eq. (49) can be written as:

$$\frac{\partial \varphi}{\partial \mathbf{x}_{p,k}} = \frac{\partial \mathbf{x}_{c,k}}{\partial \mathbf{x}_{p,k}}\left(\frac{\partial \varphi}{\partial \mathbf{x}_{c,k}} + \frac{\partial \mathbf{f}_{c,k+1}}{\partial \mathbf{x}_{c,k}}\boldsymbol{\lambda}_{k+1}\right) = \frac{\partial \mathbf{x}_{c,k}}{\partial \mathbf{x}_{p,k}}\boldsymbol{\lambda}_k \tag{51}$$

The index k in Eq. (51) can be replaced by i, thus, the sensitivity $\partial\varphi/\partial\mathbf{x}_p$ can be finalized as:

$$\frac{\partial \varphi}{\partial \mathbf{x}_{p,i}} = \frac{\partial \mathbf{x}_{c,i}}{\partial \mathbf{x}_{p,i}}\boldsymbol{\lambda}_i \tag{52}$$

To determine the Eq. (52), $\partial\mathbf{x}_{c,i}/\partial\mathbf{x}_{p,i}$ and $\partial\mathbf{x}_{c,i+1}/\partial\mathbf{x}_{c,i}$ are needed. According to Sect. 2.2.1, the $\mathbf{x}_{c,i+1}$ is a function of castable density $\mathbf{x}_{b,i+1}$, where $\mathbf{x}_{b,i+1}$ is a function of $\mathbf{x}_{c,i}$. Therefore, $\partial\mathbf{x}_{c,i+1}/\partial\mathbf{x}_{c,i}$ can be determined by the chain rule:

$$\frac{\partial \mathbf{x}_{c,i+1}}{\partial \mathbf{x}_{c,i}} = \frac{\partial \mathbf{x}_{b,i+1}}{\partial \mathbf{x}_{c,i}}\frac{\partial \mathbf{x}_{c,i+1}}{\partial \mathbf{x}_{b,i+1}} \tag{53}$$

where $\partial\mathbf{x}_{c,i}/\partial\mathbf{x}_{p,i}$, $\partial\mathbf{x}_{c,i+1}/\partial\mathbf{x}_{b,i+1}$ and $\partial\mathbf{x}_{b,i+1}/\partial\mathbf{x}_{c,i}$ can be obtained by differentiating from the Boltzmann operator of Eq. (6)&(7). The general differential form of the Boltzmann function is expressed as follows:

$$\frac{\partial X(x_1, \ldots, x_n)}{\partial x_m} = \frac{\exp\left(\overline{\alpha}x_m\right)}{\sum\limits_{e=1}^{n}\exp\left(\overline{\alpha}x_e\right)}\left[1 + \overline{\alpha}\left(x_m - X\right)\right]; m \in \{1, 2, \ldots, n\} \tag{54}$$

where X represents an element from vector $\mathbf{x}_c$ or $\mathbf{x}_b$ (i.e., $X\in\mathbf{x}_c$ or $X\in\mathbf{x}_b$), and $\overline{\alpha}\in\{\alpha_{\min}, \alpha_{\max}\}$.

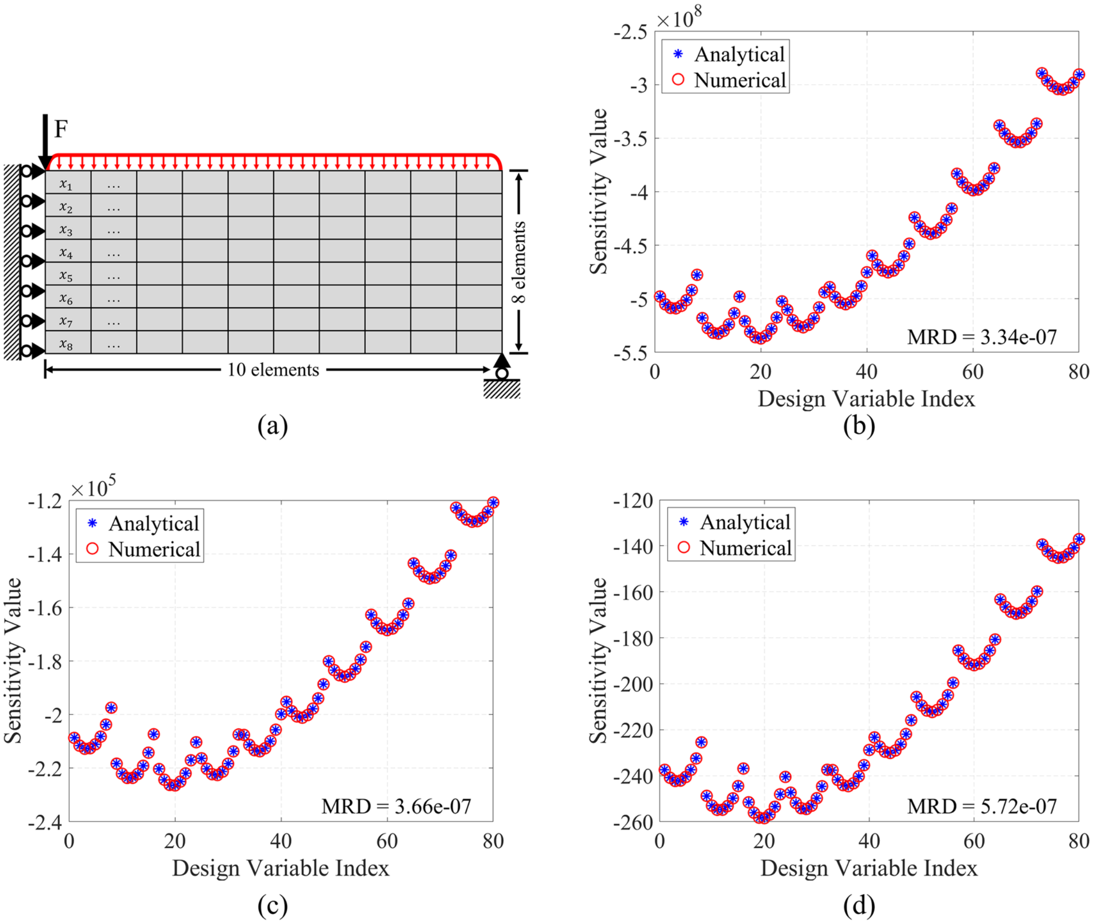

Fig. 25 a Mesh and boundary condition setup for sensitivity verification; **b–d** Analytical versus numerical sensitivity comparison for initial design density values of 0.25, 0.5, and 0.75, respectively

(3) $\partial \mathbf{x}_p / \partial \mathbf{x}_s$

Differentiation of Eq. (13) gives the sensitivity of the projected density $\mathbf{x}_p$ with respect to the smoothing density $\mathbf{x}_s$:

$$\frac{\partial \mathbf{x}_p}{\partial \mathbf{x}_s} = \frac{-\beta\left\{\tanh\left[\beta\left(\mathbf{x}_s-\eta\right)\right]^{\circ 2}-1\right\}}{\tanh(\beta\eta)-\tanh[\beta(\eta-1)]} \tag{55}$$

where “∘” represents Hadamard product (i.e., element-wise product).

(4) $\partial \mathbf{x}_s / \partial \mathbf{x}$

The sensitivity of the smoothing density $\mathbf{x}_s$ to the design density $\mathbf{x}$ is derived as:

$$\frac{\partial \mathbf{x}_s}{\partial \mathbf{x}} = \mathbf{H}_s^{\mathsf{T}} \tag{56}$$

- Verification

To validate the analytical sensitivity expressions, a numerical differentiation test is performed to demonstrate the correctness of analytical formulations. The central difference scheme is used to compare with the analytical results, which is expressed as:

$$\frac{\partial C}{\partial \mathbf{x}} \approx \frac{\Delta C}{\Delta \mathbf{x}} = \frac{C(\mathbf{x}+\Delta\mathbf{x})-C(\mathbf{x}-\Delta\mathbf{x})}{2\Delta\mathbf{x}} \tag{57}$$

where $\Delta\mathbf{x}$ is a small perturbation applied to the design variable $\mathbf{x}$, with all entries set to 10^{-6} in this case. Meanwhile, the mean relative difference (MRD) is determined to quantify the discrepancy between analytical and numerical sensitivities, which is defined as:

$$\mathrm{MRD} = \mathrm{mean}\left(\left|\left(\frac{\partial C}{\partial \mathbf{x}} - \frac{\Delta C}{\Delta \mathbf{x}}\right)\Big/\frac{\partial C}{\partial \mathbf{x}}\right|\right) \tag{58}$$

To avoid excessive data and enable clearer visualization, a relatively coarse 10 × 8 element mesh with an aspect ratio of $l_y/l_x=0.5$ is used for the verification (Fig. 25a), resulting in a total of 80 density variables. The boundary conditions are maintained consistent with Case-a of the MBB beam described in Sect. 3.1. Three sets of initial density field vectors, corresponding to values of 0.25, 0.5, and 0.75, were selected for comparative testing. The results of the analytical and numerical sensitivities are visualized in Fig. 25b–d, with the MRD displayed in the lower-right corner. Evidently, the analytical sensitivities are highly consistent with the central difference results, confirming the correctness of the derived analytical expressions.

Appendix C

Explicit expression of contact patch radius (*a*)

The explicit expression of contact patch radius (a) is an approximate solution of Eq. (23). The detailed derivation can be found in the work of Chen et al. (2023). The contact patch radius is given by:

$$a(\lambda) = \frac{1}{2}\sqrt{\frac{\omega}{\lambda}} + \frac{1}{2}\sqrt{2\sqrt{\omega\lambda} - \lambda^2} \tag{59}$$

where

$$\lambda(\delta_N) = \left(\frac{\omega}{2} + \sqrt{\frac{\omega^2}{4} + \psi\left(\delta_N\right)^3}\right)^{1/3} + \left(\frac{\omega}{2} - \sqrt{\frac{\omega^2}{4} + \psi\left(\delta_N\right)^3}\right)^{1/3} \tag{60}$$

$$\omega = \frac{4\pi\gamma(R^*)^2}{E^*} \tag{61}$$

$$\psi = \left(\frac{4R^*}{3}\right)^3 \tag{62}$$

Appendix D

Summarization of iterative optimization process

A summarization of the void ratio (1-FR), compliance of the fully solid structure (C), and compliance of the infilled structure ($\overline{C}$) during the iterative optimization process is provided in this section. As mentioned in Sect. 2.6, the initial setting of θ is 15°. This section documents the cases where the intermediate designs are generated (i.e., the θ of the final design is larger than 15°). For the final design with $\theta=15°$, detailed information can be found in the main text and not presented here.

(1) Messerschmitt-Bölkow-Blohm (MBB)

See Figs. 26, 27, and 28

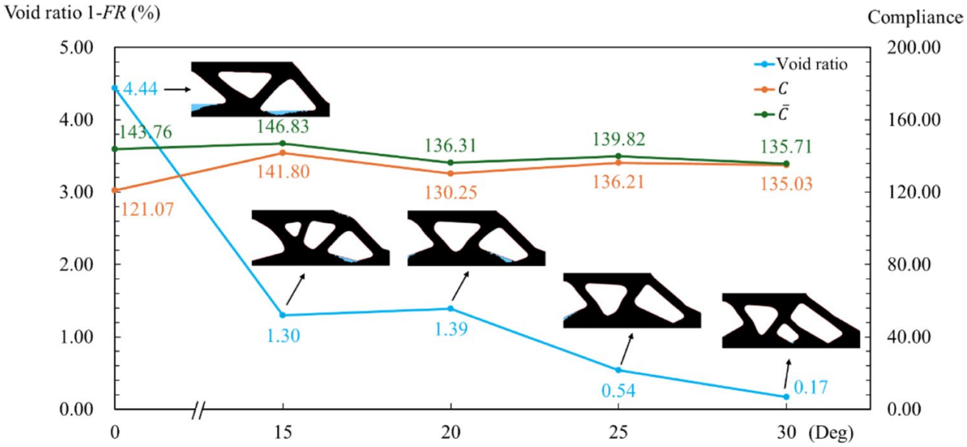

Fig. 26 Iterative optimization process of MBB beam with boundary condition *a*

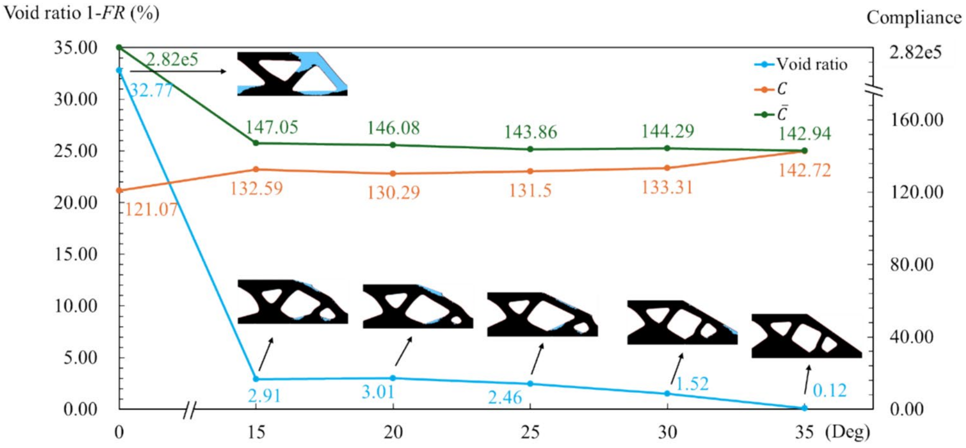

Fig. 27 Iterative optimization process of MBB beam with boundary condition *b*

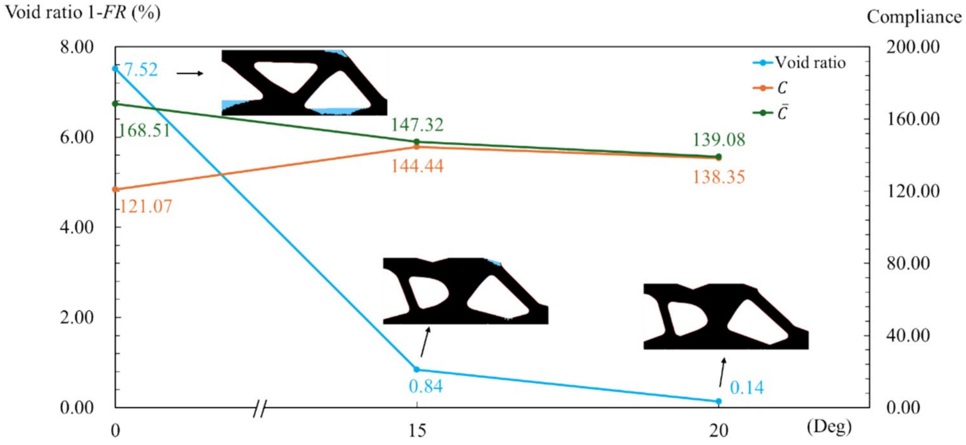

Fig. 28 Iterative optimization process of MBB beam with boundary condition *c*

(2) Cantilever beam

See 29

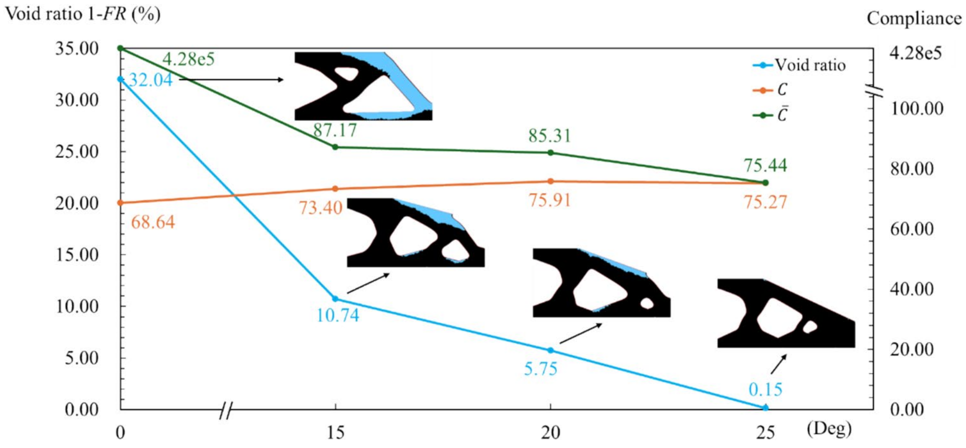

Fig. 29 Iterative optimization process of cantilever beam with boundary condition *b*

Supplementary Information The online version contains supplementary material available at https://doi.org/10.1007/s00158-025-04084-x.

Acknowledgements This work was supported by the Hong Kong Polytechnic University (P0044299 and P0051072).

Author contributions Wei Tong: conceptualization, methodology, software, investigation, validation, data curation, writing-original draft, writing-review and editing; Xiaoya Zhai: writing-review and editing, validation; Yiwei Weng: conceptualization, writing-review and editing, supervision, funding acquisition; Jun Wu: conceptualization, methodology, writing-review and editing, supervision.

Funding Open access funding provided by The Hong Kong Polytechnic University. Department of Building and Real Estate,Hong Kong Polytechnic University, P0044299, Yiwei Weng, P0051072, Yiwei Weng

Declarations

Conflict of interest The authors declare that they have no known competing financial interests or personal relationships that could have appeared to influence the work reported in this paper.

Replication of results All the essential information and parameters required for the replication of results are elaborated in detail in the paper. Further algorithm details are available upon request to the authors.

References

Aghaei-Meibodi M, Bernhard M, Jipa A, Dillenburger B (2017) The smart takes from the strong: 3D printing stay-in-place formwork for concrete slab construction. Fabricate 3:210–217. https://doi.org/10.3929/ethz-b-000237103

Amir O, Sigmund O (2013) Reinforcement layout design for concrete structures based on continuum damage and truss topology optimization. Struct Multidiscip Optim 47:157–174. https://doi.org/10.1007/s00158-012-0817-1

Andreassen E, Clausen A, Schevenels M, Lazarov BS, Sigmund O (2011) Efficient topology optimization in MATLAB using 88 lines of code. Struct Multidiscip Optim 43:1–16. https://doi.org/10.1007/s00158-010-0594-7

Asadi K and Littman ML (2017) An alternative softmax operator for reinforcement learning. International Conference on Machine Learning; 243–252.

Banfill P (2011) Additivity effects in the rheology of fresh concrete containing water-reducing admixtures. Constr Build Mater 25(6):2955–2960. https://doi.org/10.1016/j.conbuildmat.2010.12.001

Bendsoe MP and Sigmund O (2003) Topology Optimization: Theory, Methods, and Applications.

Bhavikatti S (2005) Finite element analysis.

Bogomolny M, Amir O (2012) Conceptual design of reinforced concrete structures using topology optimization with elastoplastic material modeling. Int J Numer Meth Eng 90(13):1578–1597. https://doi.org/10.1002/nme.4253

Chen J, Krengel D, Nishiura D, Furuichi M, Matuttis H-G (2023) A force–displacement relation based on the JKR theory for DEM simulations of adhesive particles. Powder Technol 427:118742. https://doi.org/10.1016/j.powtec.2023.118742

Coetzee C (2020) A Johnson-Kendall-Roberts (JKR) Contact Model.

Cundall PA, Strack OD (1979) A discrete numerical model for granular assemblies. Geotechnique 29(1):47–65. https://doi.org/10.1680/geot.1979.29.1.47

El Cheikh K, Rémond S, Khalil N, Aouad G (2017) Numerical and experimental studies of aggregate blocking in mortar extrusion. Constr Build Mater 145:452–463. https://doi.org/10.1016/j.conbuildmat.2017.04.032

Felekoğlu B, Türkel S, Baradan B (2007) Effect of water/cement ratio on the fresh and hardened properties of self-compacting concrete. Build Environ 42(4):1795–1802. https://doi.org/10.1016/j.buildenv.2006.01.012

Fernández E, Yang K-k, Koppen S, Alarcón P, Bauduin S, Duysinx P (2020) Imposing minimum and maximum member size, minimum cavity size, and minimum separation distance between solid members in topology optimization. Comput Methods Appl Mech Eng 368:113157. https://doi.org/10.1016/j.cma.2020.113157

Gaganelis G, Mark P (2019) Downsizing weight while upsizing efficiency: an experimental approach to develop optimized ultra-light UHPC hybrid beams. Struct Concr 20(6):1883–1895. https://doi.org/10.1002/suco.201900215

Gaimster R, Dixon N (2003) Self-compacting concrete. Adv Concr Technol 3:1–23. https://doi.org/10.1016/B978-075065686-3/50295-0

Guest JK (2009) Imposing maximum length scale in topology optimization. Struct Multidiscip Optim 37:463–473. https://doi.org/10.1007/s00158-008-0250-7

Hosseinpoor M, Khayat KH, Yahia A (2017) Numerical simulation of self-consolidating concrete flow as a heterogeneous material in L-Box setup: effect of rheological parameters on flow performance. Cement Concr Compos 83:290–307. https://doi.org/10.1016/j.cemconcomp.2017.07.027

Hu J, Wang K (2011) Effect of coarse aggregate characteristics on concrete rheology. Constr Build Mater 25(3):1196–1204. https://doi.org/10.1016/j.conbuildmat.2010.09.035

Isozaki A (2010) Himalayas Center. Arata Isozaki & Associates. https://isozaki.co.jp/archives/projects/himalayas/. Accessed 12 May 2025

Isozaki A (2011) Qatar National Convention Center. Arata Isozaki & Associates. https://isozaki.co.jp/archives/projects/qatar/. Accessed 12 May 2025

Jewett JL, Carstensen JV (2019) Topology-optimized design, construction and experimental evaluation of concrete beams. Autom Constr 102:59–67. https://doi.org/10.1016/j.autcon.2019.02.001

Jiao D, Shi C, Yuan Q, An X, Liu Y, Li H (2017) Effect of constituents on rheological properties of fresh concrete-A review. Cement Concr Compos 83:146–159. https://doi.org/10.1016/j.cemconcomp.2017.07.016

Jipa A, Bernhard M, Meibodi M and Dillenburger B (2016) 3D-printed stay-in-place formwork for topologically optimized concrete slabs. Proceedings of the 2016 TxA Emerging Design

+ Technology Conference; 97–107. https://doi.org/10.3929/ethz-b-000237082

Jipa A, Bernhard M, Ruffray N, Wangler T, Flatt RJ, Dillenburger B (2019) Formwork fabrication freedom for a concrete canoe. Gestão Tecnol De Projetos 14(1):25–44. https://doi.org/10.11606/gtp.v14i1.148264

Johnson KL, Kendall K, Roberts A (1971) Surface energy and the contact of elastic solids. Proc Royal Soc London A Math Phys Sci 324(1558):301–313. https://doi.org/10.1098/rspa.1971.0141

Langelaar M (2016) Topology optimization of 3D self-supporting structures for additive manufacturing. Addit Manuf 12:60–70. https://doi.org/10.1016/j.addma.2016.06.010

Langelaar M (2017) An additive manufacturing filter for topology optimization of print-ready designs. Struct Multidiscip Optim 55:871–883. https://doi.org/10.1007/s00158-016-1522-2

Li Q, Chen W, Liu S, Fan H (2018) Topology optimization design of cast parts based on virtual temperature method. Comput Aided des 94:28–40. https://doi.org/10.1016/j.cad.2017.08.002

Li Y, Hao J, Jin C, Wang Z, Liu J (2021) Simulation of the flowability of fresh concrete by discrete element method. Front Mater 7:603154. https://doi.org/10.3389/fmats.2020.603154

Li Y, Ding J, Zhang Z, Zhou X, Makvandi M, Yuan PF, Xie YM (2023) Practical application of multi-material topology optimization to performance-based architectural design of an iconic building. Compos Struct 325:117603. https://doi.org/10.1016/j.compstruct.2023.117603

Li Y, Wu H, Xie X, Zhang L, Yuan PF, Xie YM (2024) FloatArch: a cable-supported, unreinforced, and re-assemblable 3D-printed concrete structure designed using multi-material topology optimization. Addit Manuf 81:104012. https://doi.org/10.1016/j.addma.2024.104012

Liu C (2019) Matrix discrete element analysis of geology and geotechnical engineering. Science: Bejing

Liu C, Liu H, Zhang H (2021) MatDEM-fast matrix computing of the discrete element method. Earthq Res Adv 1(3):100010. https://doi.org/10.1016/j.eqrea.2021.100010

Luo Y, Wang MY, Zhou M, Deng Z (2012) Optimal topology design of steel–concrete composite structures under stiffness and strength constraints. Comput Struct 112:433–444. https://doi.org/10.1016/j.compstruc.2012.09.007

Ma G, Li Z, Wang L, Wang F, Sanjayan J (2019) Mechanical anisotropy of aligned fiber reinforced composite for extrusion-based 3D printing. Constr Build Mater 202:770–783. https://doi.org/10.1016/j.conbuildmat.2019.01.008

Mechtcherine V, Gram A, Krenzer K, Schwabe J-H, Shyshko S, Roussel N (2014) Simulation of fresh concrete flow using Discrete Element Method (DEM): theory and applications. Mater Struct 47:615–630. https://doi.org/10.1617/s11527-013-0084-7

Mindlin RD, Deresiewicz H (1953) Elastic spheres in contact under varying oblique forces. J Appl Mecha. https://doi.org/10.1115/1.4010702

Nguyen T, Roussel N, Coussot P (2006) Correlation between L-box test and rheological parameters of a homogeneous yield stress fluid. Cem Concr Res 36(10):1789–1796. https://doi.org/10.1016/j.cemconres.2006.05.001

Onyelowe K, Kontoni DN, Ebid A (2022) Simulation of self-compacting concrete (SCC) passing ability using the L-box model for sustainable buildings. IOP Conf Ser Earth Environ Sci 1123(1):012065. https://doi.org/10.1088/1755-1315/1123/1/012065

Ooms T, Vantyghem G, Tao Y, Bekaert M, De Schutter G, Van Tittelboom K and De Corte W (2022) The production of a topology-optimized 3D-printed concrete bridge. RILEM International Conference on Concrete and Digital Fabrication, 37–42. https://doi.org/10.1007/978-3-031-06116-5_6

Revilla-Cuesta V, Skaf M, Ortega-López V, Manso JM (2023) Multi-parametric flowability classification of self-compacting concrete containing sustainable raw materials: an approach to real applications. J Build Eng 63:105524. https://doi.org/10.1016/j.jobe.2022.105524

Roussel N (2007) Rheology of fresh concrete: from measurements to predictions of casting processes. Mater Struct 40(10):1001–1012. https://doi.org/10.1617/s11527-007-9313-2

Rozvany GI (2009) A critical review of established methods of structural topology optimization. Struct Multidiscip Optim 37:217–237. https://doi.org/10.1007/s00158-007-0217-0

Sato Y, Yamada T, Izui K, Nishiwaki S (2017) Manufacturability evaluation for molded parts using fictitious physical models, and its application in topology optimization. Int J Adv Manuf Technol 92(1):1391–1409. https://doi.org/10.1007/s00170-017-0218-0

Secrieru E, Mohamed W, Fataei S, Mechtcherine V (2020) Assessment and prediction of concrete flow and pumping pressure in pipeline. Cement Concr Compos 107:103495. https://doi.org/10.1016/j.cemconcomp.2019.103495

Shan Z, Yu Z, Shi J (2015) Experimental investigation of flow of fresh self-compacting concrete in improved L-box. Constr Build Mater 84:30–38. https://doi.org/10.1016/j.conbuildmat.2015.03.056

Sigmund O (2007) Morphology-based black and white filters for topology optimization. Struct Multidiscip Optim 33:401–424. https://doi.org/10.1007/s00158-006-0087-x

Sigmund O (2009) Manufacturing tolerant topology optimization. Acta Mech Sin 25:227–239. https://doi.org/10.1007/s10409-009-0240-z

Sigmund O, Maute K (2013) Topology optimization approaches: a comparative review. Struct Multidiscip Optim 48(6):1031–1055. https://doi.org/10.1007/s00158-013-0978-6

Smarslik M, Ahrens MA, Mark P (2019) Toward holistic tension-or compression-biased structural designs using topology optimization. Eng Struct 199:109632. https://doi.org/10.1016/j.engstruct.2019.109632

Søndergaard A, Feringa J, Stan F, Maier D (2018) Robotic abrasive wire cutting of polymerized styrene formwork systems for cost-effective realization of topology-optimized concrete structures. Construction Robotics 2(1):81–92. https://doi.org/10.1007/s41693-018-0016-8

Stoiber N, Kromoser B (2021) Topology optimization in concrete construction: a systematic review on numerical and experimental investigations. Struct Multidiscip Optim 64(4):1725–1749. https://doi.org/10.1007/s00158-021-03019-6

Svanberg K (1987) The method of moving asymptotes—a new method for structural optimization. Int J Numer Meth Eng 24(2):359–373. https://doi.org/10.1002/nme.1620240207

Szabó B and Babuška I (2021) Finite element analysis: Method, verification and validation.

Tong W, Wu J, Weng Y (2025) Topology optimization to eliminate cavities and internal supports in AM-produced formwork for functional structure fabrication. Struct Multidiscip Optim 68(4):76. https://doi.org/10.1007/s00158-025-04002-1

Vantyghem G, De Corte W, Shakour E, Amir O (2020) 3D printing of a post-tensioned concrete girder designed by topology optimization. Autom Constr 112:103084. https://doi.org/10.1016/j.autcon.2020.103084

Wang C, Xu B, Meng Q, Rong J, Zhao Y (2020a) Topology optimization of cast parts considering parting surface position. Adv Eng Softw 149:102886. https://doi.org/10.1016/j.advengsoft.2020.102886

Wang C, Han W, Xu B, Rong J (2023) Casting-oriented structural topology optimization with dimensional shrinkage. Appl Math Model 117:625–651. https://doi.org/10.1016/j.apm.2023.01.001

Wang F, Lazarov BS, Sigmund O (2011) On projection methods, convergence and robust formulations in topology optimization.

Struct Multidiscip Optim 43:767–784. https://doi.org/10.1007/s00158-010-0602-y

Wang W, Munro D, Wang CC, van Keulen F, Wu J (2020b) Space-time topology optimization for additive manufacturing: concurrent optimization of structural layout and fabrication sequence. Struct Multidiscip Optim 61:1–18. https://doi.org/10.1007/s00158-019-02420-6

Wu J, Clausen A, Sigmund O (2017a) Minimum compliance topology optimization of shell–infill composites for additive manufacturing. Comput Methods Appl Mech Eng 326:358–375. https://doi.org/10.1016/j.cma.2017.08.018

Wu J, Aage N, Westermann R, Sigmund O (2017b) Infill optimization for additive manufacturing—approaching bone-like porous structures. IEEE Trans Visual Comput Graphics 24(2):1127–1140. https://doi.org/10.1109/TVCG.2017.2655523

Wu J (2018) Continuous optimization of adaptive quadtree structures. Comput Aided des 102:72–82. https://doi.org/10.1016/j.cad.2018.04.008

Xia Q, Shi T, Wang MY, Liu S (2011) Simultaneous optimization of cast part and parting direction using level set method. Struct Multidiscip Optim 44(6):751–759. https://doi.org/10.1007/s00158-011-0690-3

Yan W, Cui W, Qi L (2022) DEM study on the response of fresh concrete under vibration. Granular Matter 24(1):37. https://doi.org/10.1007/s10035-021-01199-y

Zhang X, Zhang Z, Li Z, Li Y, Sun T (2020) Filling capacity analysis of self-compacting concrete in rock-filled concrete based on DEM. Constr Build Mater 233:117321. https://doi.org/10.1016/j.conbuildmat.2019.117321

Zhou M, Lazarov BS, Wang F, Sigmund O (2015) Minimum length scale in topology optimization by geometric constraints. Comput Methods Appl Mech Eng 293:266–282. https://doi.org/10.1016/j.cma.2015.05.003

Zhuang Z, Xu F, Ye J, Hu N, Jiang L, Weng Y (2024a) A comprehensive review of sustainable materials and toolpath optimization in 3D concrete printing. NPJ Mater Sustain 2(1):12. https://doi.org/10.1038/s44296-024-00017-9

Zhuang Z, Liu T, Tong W, Xu F, Weng Y (2024b) Enhancing topology optimization with colored body-fitted mesh using adaptive filter, dual re-meshing strategy, and OOP programming paradigm. Comput Methods Appl Mech Eng 432:117350. https://doi.org/10.1016/j.cma.2024.117350